

Quasi-Equilibrium and Weak Temperature Gradient Balances in an Equatorial Beta-Plane Model[Ⓞ]

FIAZ AHMED,^a J. DAVID NEELIN,^a AND ÁNGEL F. ADAMES^{b,c}

^a *Department of Atmospheric and Oceanic Sciences, University of California, Los Angeles, Los Angeles, California*

^b *Department of Climate and Space Science and Engineering, University of Michigan, Ann Arbor, Michigan*

(Manuscript received 17 June 2020, in final form 10 September 2020)

ABSTRACT: Convective quasi-equilibrium (QE) and weak temperature gradient (WTG) balances are frequently employed to study the tropical atmosphere. This study uses linearized equatorial beta-plane solutions to examine the relevant regimes for these balances. Wave solutions are characterized by moisture–temperature ratio (q – T ratio) and dominant thermodynamic balances. An empirically constrained precipitation closure assigns different sensitivities of convection to temperature (ε_t) and moisture (ε_q). Longwave equatorial Kelvin and Rossby waves tend toward the QE balance with q – T ratios of $\varepsilon_t/\varepsilon_q$ that can be ~ 1 – 3 . Departures from strict QE, essential to both precipitation and wave dynamics, grow with wavenumber. The propagating QE modes have reduced phase speeds because of the effective gross moist stability m_{eff} , with a further reduction when $\varepsilon_t > 0$. Moisture modes obeying the WTG balance and with large q – T ratios (> 10) emerge in the shortwave regime; these modes exist with both Kelvin and Rossby wave meridional structures. In the $v = 0$ case, long propagating gravity waves are absent and only emerge beyond a cutoff wavenumber. Two bifurcations in the wave solutions are identified and used to locate the spatial scales for QE–WTG transition and gravity wave emergence. These scales are governed by the competition between the convection and gravity wave adjustment times and are modulated by m_{eff} . Near-zero values of m_{eff} shift the QE–WTG transition wavenumber toward zero. Continuous transitions replace the bifurcations when $m_{\text{eff}} < 0$ or moisture advection/WISHE mechanisms are included, but the wavenumber-dependent QE and WTG balances remain qualitatively unaltered. Rapidly decaying convective/gravity wave modes adjust to the slowly evolving QE/WTG state in the longwave/shortwave regimes, respectively.

KEYWORDS: Atmosphere; Tropics; Convective adjustment; Kelvin waves; Primitive equations model

1. Introduction

Theoretical inquiries into tropical wave dynamics often begin with linearized models on the equatorial beta plane. The simplest version of these models (Matsuno 1966; Holton and Lindzen 1968)—without convective coupling—still yields modes that qualitatively resemble the observed equatorial waves in meridional structure (Kiladis et al. 2009). Quantitative differences do exist between observed and theoretical wave phase speeds, but these differences can be mitigated with the inclusion of a convective heat source (Emanuel et al. 1994). The early beta-plane models lack an analogous solution to the Madden–Julian oscillation (MJO; Madden and Julian 1971, 1994; Zhang 2005; Wang 2012) and also lack a time-varying water vapor equation.

Introducing a time-varying water vapor equation into the beta-plane wave alters the solutions in interesting ways. A prototype of this class of models was examined in Neelin and Yu (1994, hereinafter NY94) and Yu and Neelin (1994,

hereinafter YN94), with an adjustment-based convective parameterization (Betts 1986; Betts and Miller 1986). In their model, NY94 and YN94 highlighted two solutions of interest: (i) a longwave, eastward-propagating mode with a phase speed of $\sim 15 \text{ m s}^{-1}$, which they termed the “propagating deep convective mode” and (ii) a shortwave stationary mode characterized by a large humidity signal, which they termed the “moisture mode.”

The NY94 propagating deep convective mode elicited connections to the MJO because of its planetary scale and eastward propagation with a reduced phase speed (relative to dry gravity waves). The slow phase speed of this mode is governed by the gross moist stability: a parameter that had previously been introduced to study the tropical steady-state precipitation distribution and intraseasonal variability [Neelin and Held (1987), Neelin et al. (1987), and also see Raymond et al. (2009) for a review]. The propagating deep convective mode is thus convectively coupled; the dominant effect of this coupling is to damp the mode by convective adjustment (Emanuel 1993; Emanuel et al. 1994). However, this mode can be destabilized with the inclusion of wind-induced surface heat exchange (WISHE; Emanuel 1987; Neelin et al. 1987; Yano and Emanuel 1991). Notably, the connections between the NY94 propagating deep convective mode and the MJO have been revived in recent theoretical efforts (Fuchs and Raymond 2017; Raymond and Fuchs 2018) that have reemphasized the role of WISHE in MJO dynamics.

The stationary moisture mode (first highlighted in YN94) has also received much scrutiny since. Several studies (Fuchs

[Ⓞ] Supplemental information related to this paper is available at the Journals Online website: <https://doi.org/10.1175/JAS-D-20-0184.s1>.

^c Current affiliation: Department of Atmospheric and Oceanic Sciences, University of Wisconsin–Madison, Madison, Wisconsin.

Corresponding author: Fiaz Ahmed, fiaz@ucla.edu

and Raymond 2002, 2005, 2007; Raymond and Fuchs 2007) have shown that WISHE allows the otherwise stationary moisture mode to propagate, and that if the gross moist stability is negative, the otherwise damped moisture mode is unstable (Raymond and Fuchs 2009). A separate class of models (Sobel et al. 2001; Sobel 2002; Sobel and Bretherton 2003) impose the weak temperature gradient approximation (WTG) a priori, which makes moisture the only prognostic thermodynamic variable. In these WTG models, moisture modes emerge even at planetary scales, in contrast to the moisture modes in the NY94 model. The moisture modes also propagate as a result of background moisture gradients—a feature that was used to subsequently develop moisture-mode based theories of the MJO (Sobel and Maloney 2012, 2013; Adames and Kim 2016).

Despite a robust theoretical presence, the relationship between moisture modes and the observed modes of tropical variability remains ambiguous. Observation-based evidence (Roundy and Frank 2004; Yasunaga and Mapes 2012; Ahmed and Schumacher 2018; Yasunaga et al. 2019; Inoue et al. 2020) suggests that tropical waves can be broadly categorized into two groups: one dominated by moisture variability (e.g., the MJO and equatorial Rossby waves), and the other dominated by temperature variability (e.g., the convectively coupled Kelvin wave and the inertio-gravity waves). At face value, this distinction seems to suggest that moisture-dominated waves are related to moisture modes.

More recently, Adames et al. (2019) used the above distinction to suggest that a continuum of wave classes separate purely moisture-dominated modes from purely temperature-dominated modes. They argued—using scale analysis—that a single nondimensional number N_{mode} can quantify the relative importance of moisture versus temperature to any wave type and thereby place it on the continuum. In constructing their continuum, Adames et al. (2019) implicitly assumed that slow, large-scale modes of variability with large apparent humidity signatures, such as the MJO over the Indo-Pacific Warm Pool, correspond to moisture modes. However, Fuchs and Raymond (2017) argue otherwise, and suggest that the MJO—despite its large humidity signature—is a mode in which the temperature perturbations are essential to the dynamics.

These arguments exemplify the uncertainties surrounding moisture modes, which we aim to address in this study. As a first step in this process, we recognize a set of geophysically important modes that occur in complementary length scale regimes to moisture modes. These modes are adjusted by convection to a state of convective quasi equilibrium (QE; Arakawa and Schubert 1974) and are accordingly termed QE modes. Although the term QE has several interpretations (Neelin et al. 2008; Yano and Plant 2012) in this study we use the term to indicate a state of zero buoyancy, established by the consumption of buoyancy anomalies by convection. With these QE modes as foil, we now advance three conditions to identify moisture modes:

(C1) *The mode must exhibit a large humidity signature.* A useful diagnostic to measure humidity signals is the ratio of moisture to temperature perturbations (the q - T ratio γ_{qT} ; see section 2d). In a moisture mode, this ratio must greatly exceed the q - T ratio in a state of QE (γ_{QE}), i.e.,

$\gamma_{qT} \gg \gamma_{QE}$. We use a subjective q - T ratio threshold of $\gamma_{qT} \geq 3\gamma_{QE}$, that is, roughly $\gamma_{qT} \geq 10$, to express this condition.

- (C2) *The mode must obey the WTG balance at the leading order in its temperature budget;* that is, the dominant balance must be between adiabatic cooling and diabatic heating, and the temperature tendency must be a higher-order term.
- (C3) *Prognostic thermodynamic variations in the mode must be dominated by moisture.* In perturbation expansions, this condition is expressed as a requirement that the temperature tendency term must appear at a higher order than the moisture tendency term.

The conditions C1, C2, and C3 unify pieces of previously identified features of moisture modes (YN94; Sugiyama 2009; Sobel and Maloney 2012; Wolding et al. 2016; Adames et al. 2019). For instance, C2 makes it clear that moisture modes must obey the WTG balance at leading order (Sugiyama 2009), while C3 necessitates a prognostic moisture equation for the existence of moisture modes (Sobel and Maloney 2012; Sobel et al. 2014) and ensures identification of the dominant eigenmode with the moisture equation (YN94). In this study, we will employ these conditions to pursue clear theoretical identifiers for moisture and QE modes. We work with a simple model that has previously been used to study these modes: the equatorial beta-plane model of NY94. Informed by conditions C1, C2, and C3, we will characterize the modes in this model by their q - T ratios and dominant balances in the thermodynamic budgets. In the process, we will also closely examine the boundaries between QE and WTG regimes in the model.

We will utilize an observationally constrained convective closure developed from the empirical relationship between tropical precipitation and a lower-tropospheric buoyancy measure (Ahmed and Neelin 2018; Schiro et al. 2018). Figure 1 illustrates this relationship using TRMM 3B42 precipitation (Huffman et al. 2007) conditionally averaged by a buoyancy measure B_L that depends on lower tropospheric temperature and moisture profiles. The precipitation- B_L relationship in Fig. 1 subsumes other documented relationships that precipitation shares with column-integrated humidity (Bretherton et al. 2004; Peters and Neelin 2006; Ahmed and Schumacher 2015) and column-averaged temperature (Neelin et al. 2009; Kuo et al. 2018). Ahmed et al. (2020, hereinafter AAN) derived a precipitation closure using the empirical relationship in Fig. 1. Specifically, they derived estimates for the sensitivity of precipitation to both moisture and temperature fluctuations using the slope of the linear range in Fig. 1. In this study, we will employ the AAN precipitation closure to parameterize convection within the simple model. Wherever possible, we will also employ analytic approximations derived using perturbation expansions [as in NY94 and Sugiyama (2009)] to illuminate the physics distinguishing QE modes from moisture modes.

2. Model setup

a. Momentum, hydrostatic, and continuity equations

As in NY94, we begin with a system of inviscid, linearized equations on a beta-plane with vertical pressure coordinate, p :

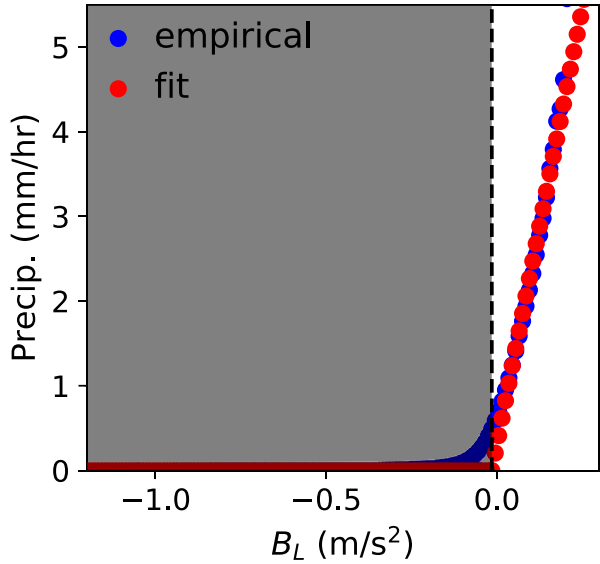


FIG. 1. Precipitation conditionally averaged by a measure of lower-tropospheric buoyancy B_L (in blue scatter). The gray shading denotes the nonprecipitating regime. A straight-line fit (red scatter) in the precipitating regime was used to derive a simple empirical precipitation closure in AAN. The figure is adapted from Fig. 2 of AAN.

$$\partial_t u - \beta y v + \partial_x \phi = 0, \tag{1}$$

$$\partial_t v + \beta y u + \partial_y \phi = 0, \tag{2}$$

$$\partial_p \phi = -\frac{R_d}{p} T, \quad \text{and} \tag{3}$$

$$\partial_x u + \partial_y v = -\partial_p \omega. \tag{4}$$

Here u , v , and ω are the linearized zonal, meridional, and vertical pressure velocities, respectively, and ϕ and T are the linearized geopotential height and temperature, respectively. The horizontal momentum equations are in (1) and (2), (3) is the hydrostatic balance, and (4) is the continuity equation. The constants β and R_d are the meridional gradient of the Coriolis parameter and the dry air gas constant, respectively. A standard set of assumptions (NY94; Neelin and Zeng 2000) including a single deep vertical structure for temperature and the rigid lid approximation are used to separate the horizontal and vertical variations in velocity and temperature such that u_1 , v_1 , ω_1 , and T_1 contain the horizontal variations in u , v , ω , and T , respectively. These horizontal variables are then assumed to follow the complex exponential representation: $u_1(x, y) = \tilde{u}_1(y) \exp(\lambda t + ikx)$, and similarly for v_1 , ω_1 , and T_1 . Here, k is the zonal wavenumber and λ is the frequency. A detailed explanation of these reduction procedures, including a plot of the vertical structures (Fig. S1), is provided in the online supplemental material. For now, we note that using these procedures (1)–(4) can be simplified to yield

$$\lambda u_1 - \beta y v_1 + ik R_d T_1 = 0, \tag{5}$$

$$\lambda v_1 + \beta y u_1 + R_d \partial_y T_1 = 0, \quad \text{and} \tag{6}$$

$$iku_1 + \partial_y v_1 = -\omega_1. \tag{7}$$

The use of a single, deep vertical structure has precedence in several simple models of tropical dynamics (NY94; Neelin and Zeng 2000; Sobel et al. 2001; Adames and Kim 2016; Adames et al. 2019). Although its formal justification works best in the QE limit (NY94), we retain its use here for the relative simplicity of the analytic approximations. The inclusion of additional vertical structures representing shallow and stratiform cloud types (Mapes 2000; Majda and Shefter 2001; Khouider and Majda 2006; Kuang 2008; Stechmann and Hottovy 2017) can induce departures from the convectively damped QE state (e.g., Lin et al. 2015; Khouider and Leclerc 2019). However, these departures can be incorporated into our analysis with the inclusion of multiple vertical profiles in the reduction procedures that yield (5)–(7) from (1)–(4).

b. Thermodynamic equations

The budgets for vertically integrated temperature \hat{T} and moisture \hat{q} are

$$\lambda \hat{T} - \omega_1 M_s - \hat{Q}_c(1 + r) = 0 \quad \text{and} \tag{8}$$

$$\lambda \hat{q} - \sigma_x u_1 + \omega_1 M_q + \hat{Q}_c = 0. \tag{9}$$

In (9), the specific humidity is scaled by the latent heat of vaporization and divided by the specific heat capacity, such that \hat{q} and \hat{T} have the same units (K kg m^{-2}). We have also assumed that \hat{q} is expressible by complex exponentials, so $\lambda \hat{T}$ and $\lambda \hat{q}$ are the temperature and moisture tendency terms. The quantity \hat{Q}_c is the column-integrated convective heating—assumed equivalent to the column-integrated moisture sink. The online supplemental material contains a full derivation of (8) and (9). The radiative feedback parameter (Fuchs and Raymond 2002; Su and Neelin 2002; Lin and Mapes 2004; Kim et al. 2015) is r , such that the term $Q_c(1 + r)$ in (8) is the diabatic heat source to the column. The gross dry stability M_s and the gross moisture stratification M_q are—as in Yu et al. (1998)—positive quantities with units of kilograms per meter squared. The terms $\omega_1 M_s$ —in (8)—and $\omega_1 M_q$ —in (9)—represent the vertical advection of the background dry static energy and moisture, respectively, by perturbations in vertical velocity.

The cumulative effects of moisture advection (Adames and Kim 2016; Adames et al. 2019) and WISHE are represented by $\sigma_x u_1$. The parameter σ_x incorporates the effects of both the background surface wind and the moisture gradients (see the online supplemental material). Note that $\sigma_x > 0$ for mean easterlies/positive zonal moisture gradient. The basic state zonal moisture gradient is assumed constant on the scale of the local wavenumber k , so caveats apply at the planetary scale with cyclic boundary conditions.

We now introduce the relative gross moist stability m :

$$m = \frac{M_s - M_q}{M_s},$$

so $M_q = (1 - m)M_s$. The dry gravity wave speed c can be expressed in terms of M_s , R_d , and the temperature vertical structure (as in Sugiyama 2009; Adames and Kim 2016):

$$c^2 = \frac{R_d M_s T_1}{\hat{T}}. \quad (10)$$

Here, c^2 , M_s , M_q , and m all implicitly contain the vertical structure information. When $v = 0$, (5), (7), and (10) can be combined to give

$$\omega_1 = -\frac{c^2 k^2 \hat{T}}{\lambda M_s}. \quad (11)$$

Radiative damping on temperature, moisture-radiative effects, and damping effects of evaporation on moisture are all easily introduced (Zeng et al. 2000), but they are omitted here to focus on the interaction with convection.

c. Precipitation closure

Our empirically informed precipitation closure is

$$\hat{Q}_c = \varepsilon_q \hat{q} - \varepsilon_t \hat{T}, \quad (12)$$

where ε_q and ε_t measure of the sensitivity of buoyancy to lower tropospheric moisture and temperature perturbations, respectively (AAN). The closure in (12) is similar to the adjustment-based Betts–Miller scheme (Betts 1986; Betts and Miller 1986). Betts–Miller type schemes are based on two separate postulates for moisture and temperature adjustment, whereas (12) emerges from a single postulate about buoyancy adjustment, with empirically constrained parameters. The dependence of precipitation on lower tropospheric temperature variations (Mapes 2000; Raymond et al. 2003; Raymond and Fuchs 2007; Kuang 2008) and moisture variations due to dilution effects are both accounted for in (12). The use of (12) implies that the base state of linearization must have $B_L > 0$; that is, it must lie within the linear regime in Fig. 1. In strict terms, this is equivalent to assuming a precipitating basic state; in practice, the background precipitation can be assumed to be arbitrarily close to zero.

Using the closure in (12) along with the definition of m in the thermodynamic budgets (8) and (9) yields

$$[\lambda + \varepsilon_t(1 + r)]\hat{T} - \omega_1 M_s - \varepsilon_q(1 + r)\hat{q} = 0 \quad \text{and} \quad (13)$$

$$(\lambda + \varepsilon_q)\hat{q} - \sigma_x u_1 + \omega_1(1 - m)M_s - \varepsilon_t \hat{T} = 0. \quad (14)$$

We now obtain a combined thermodynamic equation after eliminating \hat{q} from (13) and (14):

$$\lambda(\lambda + \varepsilon_a)\hat{T} - (\lambda + m_{\text{eff}}\varepsilon_q)M_s\omega_1 - \varepsilon_q(1 + r)(\sigma_x u_1) = 0. \quad (15)$$

In (15), we have introduced the effective convective adjustment time scale,

$$\varepsilon_a = \varepsilon_q + \varepsilon_t(1 + r),$$

that combines the cloud–radiative feedbacks along with the moisture and temperature sensitivities of precipitation. When

$r = 0$, ε_a is the convective adjustment time scale derived in AAN. In this system, ε_a can be viewed as the nominal convective adjustment time scale. We have also introduced the effective gross moist stability (Su and Neelin 2002): $m_{\text{eff}} = m(1 + r) - r$.

Note the two independent time scales in the system associated with precipitation (ε_a) and dry gravity wave propagation (ck). As will be shown later, combinations of these time scales yield important nondimensional parameters that govern interactions between convection and wave dynamics in this model.

d. Moisture–temperature ratios

A measure that will prove useful in distinguishing between QE modes and moisture modes is the q – T ratio. An expression for this ratio can be obtained by rearranging (13) and (14):

$$\gamma_{qT} = \frac{\hat{q}}{\hat{T}} = \frac{\varepsilon_t m_{\text{eff}} + \lambda(m - 1)}{\lambda + \varepsilon_q m_{\text{eff}}} + \frac{\sigma_x u_1}{\hat{T}(\lambda + \varepsilon_q m_{\text{eff}})}. \quad (16)$$

The first term on the right-hand side of (16) contains the dependence from the convective sensitivities to moisture and temperature, while the second term introduces a dependence due to WISHE/zonal moisture advection. Note that both terms can be complex, yielding a moisture–temperature zonal phase relationship that depends on the eigenvalue λ .

While detailed expressions for γ_{qT} are derived in section 3, a simple limit of (16) can already be used to introduce a characteristic property of low-frequency modes in the system. Consider motions such that $|\lambda| \ll \varepsilon_t, \varepsilon_q$. Also assume that WISHE/zonal-moisture-advection effects are negligible; that is, $\sigma_x = 0$. Under these conditions, (16) yields

$$\gamma_{qT} \approx \varepsilon_t/\varepsilon_q = \gamma_{\text{QE}}. \quad (17)$$

This ratio is simply a statement of strict QE balance, as described in AAN. The expression in (17) suggests that the q – T ratios in low-frequency modes are predominantly set by a measure of convection’s sensitivity to temperature versus moisture perturbations, which is termed γ_{QE} . For the assumed values of ε_t and ε_q in Table 1, $\gamma_{\text{QE}} = 3$. These low-frequency modes have a significant humidity signal relative to temperature, but they are convectively coupled modes in QE balance, and are therefore termed *QE modes*. This generalizes previous terminology, including propagating deep convective mode (NY94; YN94), since nonpropagating modes also exist with the same essential properties (e.g., for negative m_{eff}).

We now rewrite the precipitation closure (12) to incorporate γ_{qT} :

$$\hat{Q}_c = \varepsilon_t \hat{T} \left(\frac{\gamma_{qT}}{\gamma_{\text{QE}}} - 1 \right) = \varepsilon_q \hat{q} \left(1 - \frac{\gamma_{\text{QE}}}{\gamma_{qT}} \right). \quad (18)$$

From (18), if $\gamma_{qT} = \gamma_{\text{QE}}$ exactly, then $\hat{Q}_c = 0$; that is, a low-frequency disturbance with no driving away from pure QE cannot generate precipitation. The precipitation in these disturbances is produced by departures from QE—if convective adjustment times are fast, large precipitation can be produced by modest departures. From (16) it can also be inferred that,

TABLE 1. Parameter values used in numerical solutions.

Parameter	Description	Value	Units
c	Dry gravity wave speed	50	m s^{-1}
ε_q	Moisture sensitivity	6^{-1}	h^{-1}
ε_t	Temperature sensitivity	2^{-1}	h^{-1}
r	Cloud–radiative feedback parameter	0.2	—
σ_x	WISHE/zonal-moisture-advection parameter	1×10^{-3}	K kg m^{-3}
M_s	Gross dry stability	3.12×10^4	K kg m^{-2}
R_d	Gas constant of dry air	287.06	$\text{J kg}^{-1} \text{K}^{-1}$
β	Meridional gradient of the Coriolis parameter	2.28×10^{-11}	$\text{m}^{-1} \text{s}^{-1}$

when $\lambda \rightarrow -\varepsilon_q m_{\text{eff}}$, $\gamma_{qT} \rightarrow \infty$; that is, the mode is characterized by a humidity signature so large that temperature perturbations are negligible. Incidentally, previous studies (Sobel et al. 2001; Sugiyama 2009; Adames et al. 2019) have indeed documented that $\lambda \approx -\varepsilon_q m_{\text{eff}}$ for moisture modes.

An alternative form for γ_{qT} that will also prove useful is obtained by combining (11) and (13):

$$\gamma_{qT} = \gamma_{\text{QE}} + \frac{\lambda^2 + c^2 k^2}{\lambda \varepsilon_q (1+r)}. \tag{19}$$

If explicit expressions for λ are available, the γ_{qT} metric can be evaluated using either (16) or (19). The value of γ_{qT} can then be used to characterize wave solutions by checking if they satisfy condition C1, with QE modes having modest departures from γ_{QE} and moisture modes greatly exceeding this value. An explicit expression for γ_{qT} can also be used in (18) to evaluate conditions C2 and C3. We will seek explicit analytic approximations for λ that are available in certain limiting regimes. We first work with the simpler $v = 0$ model, since analytic expressions are easier to obtain and verify for this case, and later comment on qualitatively similar results for the $v \neq 0$ case.

3. Analytic approximations, q – T ratios, and dominant balances for the $v = 0$ case

We insert $v = 0$ into the reduced zonal momentum and continuity equations [(5) and (7)], and use them with the combined thermodynamic equation in (15) to obtain the following dispersion relationship:

$$\lambda^3 + \lambda^2 \varepsilon_a + \lambda c^2 k^2 + \varepsilon_q m_{\text{eff}} c^2 k^2 + i \varepsilon_q (1+r) \frac{\sigma_x}{M_s} k c^2 = 0, \tag{20}$$

The expression in (20) is a well-known cubic dispersion relationship (NY94; Fuchs and Raymond 2002; Sugiyama 2009; Fuchs and Raymond 2017; Adames et al. 2019) with documented numerical solutions. Perturbation expansions (NY94; Sugiyama 2009), will however, allow us to determine analytic approximations for λ in limiting cases. These approximations will allow us to fully illustrate the properties of QE and moisture modes, including the differing roles of convective adjustment in both modes.

a. Analytic approximations

We nondimensionalize $\lambda = \lambda^* ck$, where λ^* is a dimensionless frequency. While we use the gravity wave time scale ck for

nondimensionalization, we note that other choices such as the convective time scales (ε_a or ε_q) do not change our ensuing analytic approximations. We also introduce two additional dimensionless parameters:

$$\delta = \frac{ck}{\varepsilon_q m_{\text{eff}}} \quad \text{and} \tag{21}$$

$$m_r = \frac{\varepsilon_q m_{\text{eff}}}{\varepsilon_a}. \tag{22}$$

Here, δ is a key nondimensional parameter that tracks the wavenumber k by comparing the relative time scales of dry gravity wave and moisture adjustment by convection—similar to N_{mode} in Adames et al. (2019). The parameter m_r incorporates m_{eff} and the different convective sensitivities to moisture and temperature. Since $\varepsilon_a > \varepsilon_q$, $m_r < m_{\text{eff}}$; therefore, m_r can be interpreted as a *reduced gross moist stability*. This additional reduction due to the moisture and temperature sensitivities of convection proves important, so the variants of the gross moist stability and other derived parameters are summarized in Table 2.

In nondimensionalized form, the cubic dispersion relationship (20) is now

$$\lambda^{*3} \delta + \frac{\lambda^{*2}}{m_r} + \lambda^* \delta + 1 + i \xi = 0, \tag{23}$$

where we have defined a parameter associated with WISHE/zonal moisture advection ξ :

$$\xi = \frac{\sigma_x (1+r)}{M_s m_{\text{eff}} k}. \tag{24}$$

Note that ξ is not independent of k and, in fact, has a singularity at $k = 0$. It is nevertheless convenient to retain the k dependence in ξ , because realistic values of the WISHE/zonal-moisture-advection parameter σ_x (Table 1) are such that $\xi \sim O(1)$ for planetary wavenumber $k_p \sim 1$ (defining $k_p = ak$, where a is the radius of Earth). Figure S2 of the online supplemental material illustrates the k dependence of ξ . In the shortwave limit, we will use

$$\xi^* = \xi \delta m_{\text{eff}}^2$$

as the relevant nondimensional parameter to capture the effects of WISHE/zonal moisture advection. We now investigate

TABLE 2. Key derived parameters, with values based on Table 1 or maximum range considered, with a being the equatorial radius of Earth.

Parameter	Description	Value or range	Units
$\varepsilon_a = \varepsilon_t(1 + r) + \varepsilon_q$	Effective convective adjustment time scale	1.30^{-1}	h^{-1}
$\gamma_{\text{QE}} = \varepsilon_t/\varepsilon_q$	Moisture-temperature ratio in strict QE	3	—
$m = (M_s - M_q)/M_s$	Relative gross moist stability	from 0 to 1	—
$m_{\text{eff}} = m(1 + r) - r$	Effective gross moist stability	from -0.2 to 1	—
$m_r = (\varepsilon_q/\varepsilon_a)m_{\text{eff}}$	Reduced gross moist stability	from -0.043 to 0.22	—
$\delta = ck/\varepsilon_q m_{\text{eff}}$	Parameter for perturbation expansion	from 0 to ∞	—
$\varepsilon_q/\varepsilon_a = [\gamma_{\text{QE}}(1 + r) + 1]^{-1}$	Ratio governing m_r	4.6^{-1}	—
$\varepsilon_a a(2c)^{-1}$	Gravity wave emergence wavenumber (at $m_{\text{eff}} = 0$)	13.6	—
$2(\varepsilon_a \varepsilon_q)^{1/2} a c^{-1} m_{\text{eff}}^{1/2}$	QE-WTG transition wavenumber ($m_{\text{eff}} < 0.51$)	$25.4 \times m_{\text{eff}}^{1/2}$	—

the analytic approximations for the solutions of (20) under different wavenumber limits.

1) LONGWAVE/FAST ADJUSTMENT BALANCES

For a fixed m_{eff} , consider the limit of small δ . This can occur by small k or large ε_q . For realistic parameters, a combination of both factors aids the accuracy of the analytic solution relative to numerical results. For brevity we refer to this as the longwave regime hereinafter. We look for solutions in this limit by expanding λ^* in a perturbation series with δ as the small parameter:

$$\lambda^* = \lambda^{(-1)}\delta^{-1} + \lambda^{(0)} + \delta\lambda^{(1)} + \delta^2\lambda^{(2)} + \delta^3\lambda^{(3)} + \dots \quad (25)$$

Here $\lambda^{(-1)}, \lambda^{(0)}, \lambda^{(1)}$, and so on are nondimensional variables of $O(1)$ that must be solved for in order to reconstruct λ^* . Note that both NY94 and Sugiyama (2009) employed similar perturbation expansions to derive solutions in limiting regimes. Substituting (25) in (23), grouping by order of growth, and neglecting terms smaller than $O(\delta^3)$, we get two eastward-propagating solutions (λ_1 and λ_2). We also obtain a westward-propagating solution, which we neglect because it does not decay away from the equator. The full derivation involving perturbation expansions is included in the online supplement material, and we only present the solutions in the main text. We now examine λ_1 and λ_2 :

$$\lambda_1 = -ick\sqrt{m_r}\sqrt{1 + i\xi} - \frac{c^2k^2[1 - m_r(1 + i\xi)]}{2\varepsilon_a} + O(k^3) \quad \text{and} \quad (26)$$

$$\lambda_2 = -\varepsilon_a + \frac{c^2k^2}{\varepsilon_a}[1 - m_r(1 + i\xi)] + O(k^3). \quad (27)$$

The mode, λ_2 is damped at the nominal convective adjustment time scale, ε_a , so we infer that the convective adjustment in the longwave regime is primarily accomplished through this mode. This mode is weakly propagating due to the WISHE/zonal-moisture-advection term, ξ . For instance, this mode has phase speeds of approximately less than 2 m s^{-1} for $k_p < 5$.

The mode λ_1 is the ‘‘propagating deep convective mode’’ from NY94 and the ‘‘WISHE moisture mode’’ from Fuchs and Raymond (2017). Dynamically, this mode shares properties with the convectively coupled Kelvin wave, in that it propagates

due to temperature variations. We shall therefore refer to this mode as a long Kelvin wave, even though it must be recognized that its properties are modified by the presence of both WISHE and zonal moisture advection, and by the coupling to convection. The quantity $m_r(1 + i\xi)$ in (26) suggests itself as another variant of the gross moist stability that includes the effects of WISHE/zonal moisture advection as well as the reduced static stability.

To obtain the phase speeds and growth rates for λ_1 , we now write

$$\sqrt{1 + i\xi} = A + \text{sign}(\xi)iB, \quad (28)$$

where

$$A(k) = \frac{1}{\sqrt{2}} \left(\sqrt{\sqrt{1 + \xi^2} + 1} \right) \quad \text{and} \quad (29)$$

$$B(k) = \frac{1}{\sqrt{2}} \left(\sqrt{\sqrt{1 + \xi^2} - 1} \right). \quad (30)$$

Here, ξ, A , and B are real, positive, and dependent on k : they vary as $O(k^{-1})$ for $k < 1$ with a singularity at $k = 0$, and as $O(1)$ for $k > 1$ (see Fig. S2 in the online supplemental material). We already see from (26) and (28) that this mode has a positive contribution to the growth rate if the $\xi > 0$. The growth rates and phase speed in (26) can be explicitly extracted after neglecting terms of $O(k^3)$:

$$\text{Re}(\lambda_1) = ck\sqrt{m_r} \text{sign}(\xi)B - \frac{c^2k^2(1 - m_r)}{2\varepsilon_a} \quad \text{and} \quad (31)$$

$$c_1 = \frac{-\text{Im}(\lambda_1)}{k} = c\sqrt{m_r}A - c^2 \frac{\sigma_x \varepsilon_q (1 + r)}{M_s 2\varepsilon_a^2}, \quad (32)$$

where we have used (24)—the definition for ξ —in (32), which eliminates the k dependence from the second right hand side term of (32). From (31), we see that this mode has positive growth rates for small k when $\xi > 0$. With increasing wavenumbers the $O(k^2)$ term surpasses the $O(k)$ term, and this mode experiences scale-selective damping.

From (32), we see that this mode propagates eastward for small wavenumbers with a phase speed that is dependent on m_r and A . It evident that this mode travels slower than dry gravity

waves by a factor of $(m_r)^{1/2}A$. For $k_p \sim 1$, $A \sim 1$ such that the primary influence on the slow phase speeds is from the term $(m_r)^{1/2}$. The retarding effects on convectively coupled waves due to a reduced effective static stability are well known (NY94; Emanuel et al. 1994; Tian and Ramanathan 2003; Frierson 2007; Raymond et al. 2009). However, (32) shows that *there is additional reduction in the effective static stability because of convection's sensitivity to both temperature (ε_t) and moisture (ε_q) perturbations*. The parameter values from Table 1 yield $c_1 \approx 8 \text{ m s}^{-1}$ for $k_p = 2$. With this additional mechanism of wave retardation, convectively coupled QE modes appear to travel at speeds closer to observed MJO phase speeds. For an alternate set of vertical structure assumptions used in AAN ($\varepsilon_q^{-1} = 4 \text{ h}$; $\varepsilon_t^{-1} = 3 \text{ h}$), this mode is faster, with $c_1 \approx 13 \text{ m s}^{-1}$.

We now examine the moisture–temperature ratio of this mode by using (26) in the expression for γ_{qT} (19) to get

$$\gamma_{qT1} = \gamma_{QE} + i\delta\sqrt{m_r}\frac{\varepsilon_a}{\varepsilon_q}\left[\frac{1 - m_r(i\xi + 1)}{(1+r)\sqrt{i\xi + 1}}\right] + O(\delta^2). \quad (33)$$

At the leading order, as $\delta \rightarrow 0$, the q – T ratio of this mode approaches γ_{QE} , so this mode can be characterized as a QE mode. Note that *a substantial portion of the humidity variations in this mode are expended in maintaining the leading-order QE state*. The departures from γ_{QE} , including the WISHE/zonal-moisture-advection effects enter at $O(\delta)$ and grow with increasing wavenumber. These departures could potentially endow this mode with a significant humidity signature even at planetary scales, but the $O(\delta)$ departures from γ_{QE} in (33) do not satisfy condition C1, which demands that $\gamma_{qT} \gg \gamma_{QE}$. To test if this mode satisfies C2 and C3, we first compute the leading-order convective heating using (33) in the precipitation closure (12):

$$\hat{Q}_{c1} = i\varepsilon_a \hat{T}\sqrt{m_r}\left[\frac{1 - m_r(i\xi + 1)}{(1+r)\sqrt{i\xi + 1}}\right] \delta + O(\delta^2). \quad (34)$$

The convective heating enters at $O(\delta)$, since the heating in the leading-order QE state is zero. With (34), we examine the dominant balances in the temperature budget after using the expressions for ω_1 —[(11)]—and λ_1 —[(26)]—in the general temperature budget (8):

$$\underbrace{-ickm_r(1+i\xi)\hat{T}}_{T \text{ tendency}} + \underbrace{ick\hat{T}}_{\text{adiabatic cooling}} = \underbrace{ick\hat{T}[1 - m_r(i\xi + 1)]}_{\text{diabatic heating}}. \quad (35)$$

The moisture budget is similarly obtained after using (11) and (26) in (9):

$$\underbrace{-ick\gamma_{QE}\hat{T}m_r(1+i\xi)}_{q \text{ tendency}} + \underbrace{-ck\hat{T}\frac{\xi m_{\text{eff}}}{1+r}}_{\text{WISHE/zonal moisture advection}} + \underbrace{-ick(1-m)\hat{T}}_{\text{moisture convergence}} = \underbrace{-ick\hat{T}\left[\frac{1 - m_r(i\xi + 1)}{1+r}\right]}_{\text{precipitation}}. \quad (36)$$

For the mode λ_1 , the temperature budget in (35) and the moisture budget in (36) have full balances at $O(k)$. More importantly, the temperature tendency is a leading-order term (for nonzero m_r). This mode therefore fails to satisfy C2 and C3. Despite having a potentially large q – T ratio due to the WISHE/zonal-moisture-advection effects in (36), and a prognostic moisture equation, this QE mode is not a moisture mode because of strong time-varying temperature perturbations. Moreover, the temperature budget (35) implies that this mode would not exist if the WTG approximation is imposed a priori on the system, that is, if the temperature tendency is neglected.

2) SHORTWAVE BALANCES

In the shortwave limit, that is, when $k \rightarrow \infty$, the parameter $\delta \rightarrow \infty$. In this limit, $\xi \sim O(k^{-1})$, so we rewrite the non-dimensionalized cubic dispersion relationship (23):

$$\lambda^*{}^3\delta + \frac{\lambda^*{}^2}{m_r} + \lambda^*\delta + 1 + i\frac{\xi^*}{\delta m_{\text{eff}}^2} = 0, \quad (37)$$

where $\xi^* = \xi\delta m_{\text{eff}}^2$ is now $O(1)$. From (37), it is clear that the WISHE/zonal-moisture-advection effects are weak—of $O(\delta^{-1})$ —in this shortwave limit. We now expand λ^* in the small parameter, δ^{-1} :

$$\lambda^* = \Lambda^{(0)} + \delta^{-1}\Lambda^{(1)} + \delta^{-2}\Lambda^{(2)} + \delta^{-3}\Lambda^{(3)} + \dots \quad (38)$$

Here the nondimensional variables $\Lambda^{(0)}$, $\Lambda^{(1)}$, $\Lambda^{(2)}$, and so on, are analogous to $\lambda^{(0)}$, $\lambda^{(1)}$, $\lambda^{(2)}$, and so on, in the longwave regime. Perturbation expansion again yield two valid solutions, λ_3 and λ_4 :

$$\lambda_3 = -\left(\frac{\varepsilon_a - \varepsilon_q m_{\text{eff}}}{2}\right) - ick + O(\delta) \quad \text{and} \quad (39)$$

$$\lambda_4 = -\varepsilon_q m_{\text{eff}} - \frac{i\xi^*}{\delta} \frac{\varepsilon_q}{m_{\text{eff}}} + O(\delta^{-2}). \quad (40)$$

The mode λ_3 travels at the dry gravity wave speed but is damped by the coupling to convection. Following the terminology of Fuchs and Raymond (2002), we will refer to this mode as a gravity wave. This mode could also just as easily be termed a short Kelvin wave, since the dispersion curves for both inertio-gravity and Kelvin waves converge in the shortwave limit (Matsuno 1966). This mode is heavily damped and will play a role in the adjustment process in this shortwave regime.

The mode λ_4 is convectively damped at the leading order (if $m_{\text{eff}} > 0$) and is weakly propagating because of the WISHE/zonal-moisture-advection term at $O(\delta^{-1})$. We now compute the q – T ratio for λ_4 by using (40) in the expression for γ_{qT} , (19):

$$\gamma_{qT4} = \gamma_{QE} - m_{\text{eff}}\frac{(\delta^2 + 1)}{(1+r)} + O(\delta^{-1}). \quad (41)$$

We now see that the q – T ratio for this mode grows quadratically with δ and therefore with wavenumber. Since δ is a large parameter, it follows that $\gamma_{qT} \gg \gamma_{QE}$. Clearly this mode has a large q – T ratio and satisfies C1. To verify the dominant balances in the thermodynamic budgets, we first obtain the

leading-order convective heating term after using (41) in the rewritten expression for the precipitation closure, (18):

$$\hat{Q}_{c4} = -\varepsilon_q \hat{T} m_{\text{eff}} \frac{(\delta^2 + 1)}{(1+r)} \approx \varepsilon_q \hat{q}, \quad (42)$$

where we have used the fact that $\gamma_{qT4} \gg \gamma_{QE}$ (for large δ) to obtain the last equality. The last term on the right hand side of (42) is the moisture-only precipitation closure often employed in simple models of tropical disturbances (Sobel and Maloney 2012, 2013; Sukhatme 2014; Adames and Kim 2016; Wang et al. 2016; Stechmann and Hottovy 2017). It is clear that the neglect of the temperature fluctuations to precipitation is formally justified in the shortwave regime, for this particular mode.

With the convective heating in (42), we now obtain the leading-order temperature and moisture budgets for λ_4 using (40) in the general temperature and moisture budgets: (8) and (9), and the expression for ω_1 in (11):

$$\underbrace{-\varepsilon_q^2 m_{\text{eff}}^2 \hat{T}}_{T \text{ tendency}} - \underbrace{c^2 k^2 \hat{T}}_{\text{adiabatic cooling}} = - \underbrace{\hat{T}(c^2 k^2 + \varepsilon_q^2 m_{\text{eff}}^2)}_{\text{diabatic heating}} \quad \text{and} \quad (43)$$

$$\underbrace{(-\varepsilon_q m_{\text{eff}}) \hat{q}}_{q \text{ tendency}} + \underbrace{i \xi^* \frac{\varepsilon_q^2 m_{\text{eff}}^2}{ck} \hat{q}}_{\text{WISHE/zonal moisture advection}} - \underbrace{\varepsilon_q \hat{q}(1 - m_{\text{eff}})}_{\text{moisture convergence}}$$

$$= \underbrace{-\varepsilon_q \hat{q}}_{\text{precipitation}} + \underbrace{O(k^{-1})}_{\text{higher order terms}}. \quad (44)$$

In (43), the dominant balance—at $O(k^2)$ —is between the adiabatic cooling and the diabatic heating terms, while the temperature tendency is only of $O(1)$. This mode therefore satisfies C2. The WISHE/zonal-moisture-advection term in (44) is not a leading-order term and is instead balanced by higher-order terms at $O(k^{-1})$. From (41), (43), and (44), we clearly see that the moisture tendency term is larger than the temperature tendency term by $O(\delta^2)$; this mode therefore satisfies C3. This mode satisfies all three conditions outlined in section 1 and can now justifiably be termed a moisture mode. A consequence of the small temperature perturbations in the moisture mode is that the precipitation can be discerned solely from the moisture perturbations, as implied by (42).

Note that Sugiyama (2009) also used perturbation expansions to derive a similar dispersion relationship to (40). This relationship can also be derived by imposing the WTG approximation a priori on the system (Sobel et al. 2001; Adames and Kim 2016; Fuchs and Raymond 2017). The results of this section clearly show that the WTG balance in (43) only emerges in the shortwave limit—when $m_{\text{eff}} > 0$ —for one particular mode, λ_4 . One way to allow WTG moisture modes to emerge even at planetary scales (with finite m_{eff}) is to take $c \rightarrow \infty$, that is, assume infinite dry gravity wave speeds. From the definition of δ in (21), it can be seen that this limit of infinite gravity wave speed—which implies $\delta \rightarrow \infty$ —will yield the WTG moisture mode solution for all length scales. *The finiteness of the dry gravity speed*

therefore places an upper bound on the length scale of the WTG moisture mode.

At this juncture, it is worth pointing out the similarities between δ and the nondimensional number N_{mode} introduced in Adames et al. (2019), which can be written as

$$N_{\text{mode}} = \frac{\varepsilon_q \lambda}{c^2 k^2} = \delta^{-1} \left(\frac{\lambda}{m_{\text{eff}} ck} \right). \quad (45)$$

Note that, since $\lambda = \lambda(k)$, N_{mode} is not formally a parameter. With expressions for λ from perturbation expansions, N_{mode} can be expressed in terms of the nondimensional parameter δ . Adames et al. (2019) showed that taking the different limits of N_{mode} yield the dispersion relationships characterizing low frequency convectively coupled waves (when $N_{\text{mode}} \rightarrow \infty$) and moisture modes (when $N_{\text{mode}} \rightarrow 0$). It can be verified from (45) that these limits correspond to the longwave ($\delta \rightarrow 0$) and shortwave ($\delta \rightarrow \infty$) limits, respectively, when m_{eff} is fixed.

3) SMALL GROSS MOIST STABILITY

The preceding analyses assumed fixed values for m_{eff} . It is also important to consider the case when $m_{\text{eff}} \rightarrow 0$ for a fixed wavenumber. This case can be handled with small modifications to (37):

$$\lambda^* \delta + \lambda^* \delta \frac{\varepsilon_a}{ck} + \lambda^* \delta + 1 + i \frac{\xi^*}{\delta} = 0. \quad (46)$$

For a fixed wavenumber, $\delta \rightarrow \infty$ as $m_{\text{eff}} \rightarrow 0$. This large δ limit is the similar to the shortwave limit. The valid solutions to (46) from perturbation expansions in this limit are

$$\lambda_5 = - \left(\frac{\varepsilon_a \pm \sqrt{\varepsilon_a^2 - 4c^2 k^2}}{2} \right) + O(m_{\text{eff}}) \quad \text{and} \quad (47)$$

$$\lambda_6 = -\varepsilon_q m_{\text{eff}} - \frac{\varepsilon_q^2 m_{\text{eff}}^2}{ck} \left(i \xi^* + \frac{\varepsilon_a}{ck} \right) + O(m_{\text{eff}}^3). \quad (48)$$

Here, λ_5 represents a damped mode that is stationary for $k \leq \varepsilon_a/(2c)$ and propagating for $k > \varepsilon_a/(2c)$. In the limit of small k , this mode is damped at the convective adjustment time scale ε_a , similar to the weakly propagating mode in (27). In the limit of large k , this mode propagates at the dry gravity wave speed, similar to (39). The dominant adjustment process in this limit of small m_{eff} is therefore wavenumber dependent and can be accomplished by either convection or gravity waves. The pertinent threshold wavenumber that separates the regimes of convective and gravity wave adjustment is given by $\varepsilon_a/(2c)$.

The mode represented by λ_6 is the same as the WTG moisture mode (λ_4) to the leading order. Since $m_{\text{eff}} \rightarrow 0$, we see from (48) that this mode is nearly neutral and stationary. This mode shares other properties with the WTG moisture mode, including the large q - T ratio from (41), the convective heating from (42), and the leading-order thermodynamic balances from (43) and (44). This mode clearly satisfies C1 and C2. We see from (44) that dominant balance in the moisture budget is simply between precipitation and moisture convergence, with the moisture tendency a higher-order term in the moisture budget. However, the temperature tendency is still smaller

TABLE 3. Results of the moisture mode test outlined in section 1 for important modes under three different regimes.

Regime	Condition 1: Large q - T ratio	Condition 2: WTG temperature balance	Condition 3: Prognostic moisture	Dominant adjustment	Verdict
Small k	No ($\gamma_{qT} \approx \gamma_{QE}$)	No	No	Convection	Fail; a QE mode
Large k	Yes ($\gamma_{qT} \gg \gamma_{QE}$)	Yes	Yes	Gravity waves	Pass
$m_{\text{eff}} \rightarrow 0$	Yes ($\gamma_{qT} \gg \gamma_{QE}$)	Yes	Yes	Convection: if $k \leq \varepsilon_d(2c)$; Gravity waves: if $k > \varepsilon_d(2c)$	Pass, but in a narrow range of m_{eff}

than the moisture tendency by $O(m_{\text{eff}})$, so this mode also satisfies C3 and can be termed a moisture mode.

The moisture mode can therefore arise at any length in the limit of vanishing m_{eff} , but a few key differences from the shortwave moisture mode in (40) must be noted. The dominant adjustment in the $k \rightarrow \infty$ case is performed by the gravity waves, λ_3 in (39). In contrast, the dominant adjustment in the $m_{\text{eff}} \rightarrow 0$ case can be performed either by convection or by gravity waves, depending on the threshold wavenumber, $\varepsilon_d(2c)$. When the length scale of the mode is such that $k \leq \varepsilon_d(2c)$, small departures of m_{eff} away from zero can rapidly change the limit from $\delta \rightarrow \infty$ to $\delta \rightarrow 0$ and yield QE modes, as in the expression for λ_1 in (26). For length scales such that $k \leq \varepsilon_d(2c)$, the perturbations to m_{eff} away from zero do not greatly perturb the $\delta \rightarrow \infty$ limit, such that the mode remains a moisture mode. The planetary-scale, low m_{eff} moisture mode therefore only exists in a narrow range of m_{eff} values close to zero. This narrow-range sensitivity of this mode will be further highlighted with numerical solutions in the section 4. Table 3 summarizes the conditions satisfied by the different modes in the $v = 0$ beta-plane model, and the dominant adjustment processes, under the different limits considered in this section.

b. Adjustment to QE and WTG

In AAN, a convectively driven system without wave dynamics was shown to adjust to a state of QE. This state in the moisture-temperature phase space (the q - T space) can be identified as the set of points that have $\gamma_{qT} = \gamma_{QE}$. It is now instructive to examine how this convective adjustment process is altered in the presence of wave dynamics. For this exercise, γ_{qT} values for the different modes are interpreted as eigenvectors in the q - T space with the respective eigenvalues given by the analytic expressions for λ . A propagator matrix is then constructed from these eigenvalue-eigenvector pairs to represent the evolution of \hat{q} and \hat{T} in q - T space. Since the propagator for the wind field is not included, the matrix does not fully capture the evolution in phase space. However, the dynamics are implicitly present in the eigenvalue-eigenvector pairs used to construct the matrix (see the online supplemental material for more details). We emphasize that this propagator matrix is utilized as a conceptual tool to highlight the mechanics of adjustment, similar to Fig. 4 in AAN.

Since we wish to depict the adjustment process, only stable solutions are considered by using a positive value of m_{eff} ($=0.1$) and turning off WISHE/zonal-moisture-advection effects ($\xi = 0$). We consider two fixed wavenumbers in the longwave ($k_p = 2$) and shortwave ($k_p = 20$) regimes. The parameter values from Table 1 are plugged into the analytic approximations for

γ_{qT} and λ to numerically evaluate the eigenvalues and eigenvectors. The propagator matrix is then used to evolve five arbitrary initial perturbations in the \hat{q} - \hat{T} plane. The ensuing evolution of the in-phase components (real parts) of \hat{q} and \hat{T} are depicted in Fig. 2.

Perturbations in the longwave regime (Fig. 2a) are rapidly adjusted close to the QE line by the heavily damped mode in (27). This fast adjustment process is similar to the convective adjustment depicted in Fig. 4 of AAN, i.e., the evolution dictated by the precipitation closure in (12) with negligible modification by dynamics brings the system close to the QE line. The slower adjustment by the damped QE mode, i.e., (26) with $\xi = 0$, proceeds toward the base state of linearization, until both the \hat{T} and \hat{q} perturbations are erased. Since all the modes are damped, the base state of linearization is an attractor. The slope of the slow adjustment direction is close to the slope of the QE line (where $\gamma_{qT} = \gamma_{QE}$). This slope is wavenumber dependent and approaches γ_{QE} as $k \rightarrow 0$.

In the short wavelength regime (Fig. 2b), perturbations are rapidly adjusted by the gravity waves in (39). The slow adjustment direction in this regime is marked by a near invariance in the \hat{T} direction. The slope of the slow adjustment direction, like in the longwave regime, is also wavenumber dependent and approaches the WTG line (the vertical) as $k \rightarrow \infty$.

Reintroducing WISHE/zonal moisture advection yields an unstable solution in the longwave regime, while using a negative value of m_{eff} yields an unstable solution in both the longwave and shortwave regimes. The phase diagrams in the presence of these unstable solutions show amplification—instead of decay—along the slow eigenvector direction, and the base state of linearization morphs into a saddle point (not shown).

The phase diagram in Fig. 2 illustrates the dichotomy between the longwave QE modes and the shortwave WTG moisture modes. Figure 2 also suggests that the slow adjustment direction transitions from the QE direction toward the WTG direction, as the wavenumber increases. The nature of this transition (e.g., continuous vs discontinuous) is unknown at this point. To further examine the details of this transition, we now turn to numerical solutions.

4. Numerical solutions to dispersion curves

a. Growth rates and frequency

The cubic dispersion relationship in (20) is numerically solved using a root solver with the parameter values in Table 1. The resulting growth rates and frequencies for the valid (stationary or eastward propagating) solutions are displayed in

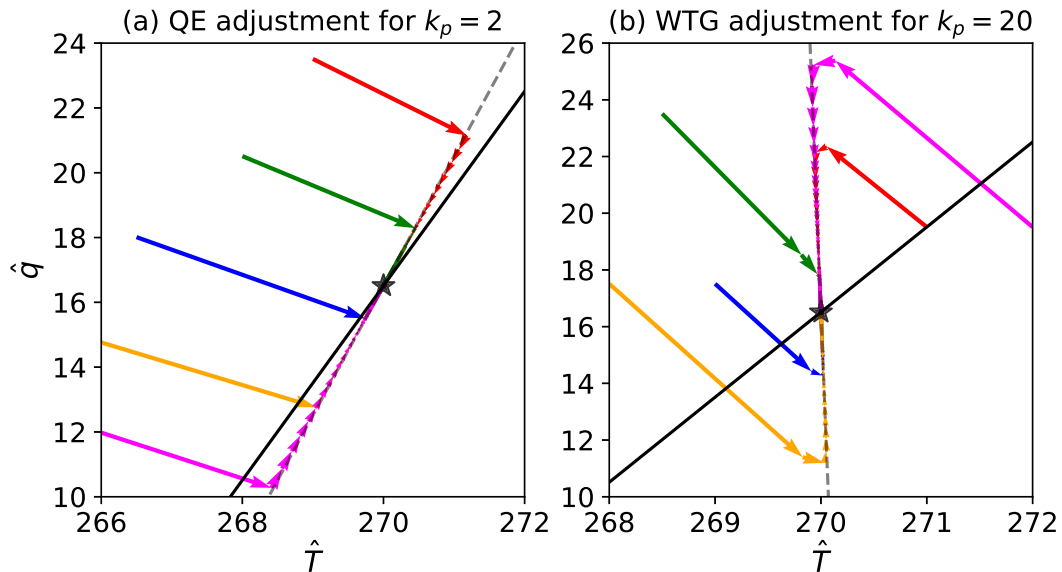


FIG. 2. Schematic illustrating the adjustment process in the $\hat{q} - \hat{T}$ plane for the (a) QE and (b) WTG moisture mode regimes, for fixed planetary wavenumbers ($k_p = ka$). The bases of the different colored arrows indicate five different initial conditions from which the solutions are allowed to evolve, with longer arrows indicating faster adjustment. The star symbol marks the base state of linearization. The solid black line is the QE line, and the dashed gray line denotes the slow direction of adjustment. Both \hat{q} and \hat{T} are normalized by an arbitrary tropospheric pressure depth of 850 hPa so that they have units in kelvins.

Fig. 3, for cases with (Figs. 3a,b) and without (Figs. 3c,d) WISHE/zonal moisture advection. Note that similar numerical solutions are also found in previous studies (YN94; Fuchs and Raymond 2002, 2017; Adames et al. 2019), who primarily focused on the stability and phase speeds of the solutions. Our focus here will lie on the transition between longwave QE modes and the shortwave WTG moisture modes.

In Fig. 3, the analytic approximations track the numerical solutions quite closely for a long range of wavenumbers. In Fig. 3a, the QE mode solution in the longwave regime—from (26)—tracks the numerical solution from $k_p = 0$ to $k_p \sim 2.5$ for $m_{\text{eff}} = -0.1$ and to $k_p \sim 5$ for $m_{\text{eff}} = 0.1$. The WTG moisture mode in the shortwave regime—from (40)—extends to $k_p \sim 10$ from $k_p \rightarrow \infty$. More importantly, the QE and the WTG moisture modes in Fig. 3a appear to lie on the same solution branch. In other words, the QE mode continuously transitions to the WTG moisture mode as k varies from 0 to ∞ . A cusp in the growth rates appears to separate the QE mode solutions from the WTG moisture mode solutions; this cusp is particularly noticeable for $m_{\text{eff}} = 0.3$ and $m_{\text{eff}} = 0.5$. The location of this cusp can therefore be interpreted as the wavenumber that marks the transition between the QE mode and the WTG moisture mode. In Fig. 3a, this QE–WTG transition wavenumber appears to increase with m_{eff} .

In Fig. 3b, the phase speed of the QE mode rapidly reduces away from the singularity at $k_p = 0$ toward the reduced gravity wave speed $[c(m_p)^{1/2}]$ at $k_p \sim 1$. The frequency of the QE solution branch (inset in Fig. 3b) resembles the observed MJO wavenumber–frequency relationship (Wheeler and Kiladis 1999; Kiladis et al. 2009) for $m_{\text{eff}} = 0.1$. For larger values of m_{eff} , the phase speeds increase [as $(m_{\text{eff}})^{1/2}$], such that the

wavenumber–frequency relationship resembles the observed Kelvin wave spectrum. The QE mode is clearly dispersive, but the dispersive character (denoted by the maxima in frequency) is only evident for wavenumbers close to the QE–WTG transition wavenumber.

From Fig. 3b, it can be seen that the propagating QE modes gradually transition to the near-stationary WTG moisture modes for wavenumbers larger than the apparent QE–WTG transition wavenumber. Figure 3b also highlights the emergence of propagating modes for $k_p \gtrsim 15$, which then asymptote to the dry gravity speed. In this system, gravity waves only exist for waves shorter than this wavenumber cutoff. This wavenumber cutoff for gravity wave emergence also exhibits a dependence on m_{eff} . Interestingly, Fuchs and Raymond (2002) and Fuchs and Raymond (2005) also noted the emergence of gravity waves in their numerical solutions, but found that their transition wavenumber was smaller than $k_p = 1$. This result is due to their choice of the convective adjustment time scale, as we will see in the next section. Relatedly, YN94 also encountered multiple gravity wave transitions corresponding to different vertical structures.

Solutions in the absence of WISHE/zonal moisture advection (Figs. 3c,d) are obtained by setting $\sigma_x = 0$ into (20) for numerical solutions and $\xi = 0$ for analytical solutions. Without WISHE/zonal moisture advection, when $m_{\text{eff}} > 0$, the transition from propagating longwave QE modes to the stationary shortwave WTG moisture modes occurs at distinct points along the solution branches. As the wavenumber is increased from zero, the propagating QE solution bifurcates at an intermediate wavenumber into two stationary solutions: one of which is the WTG moisture mode. For instance, for $m_{\text{eff}} = 0.1$,

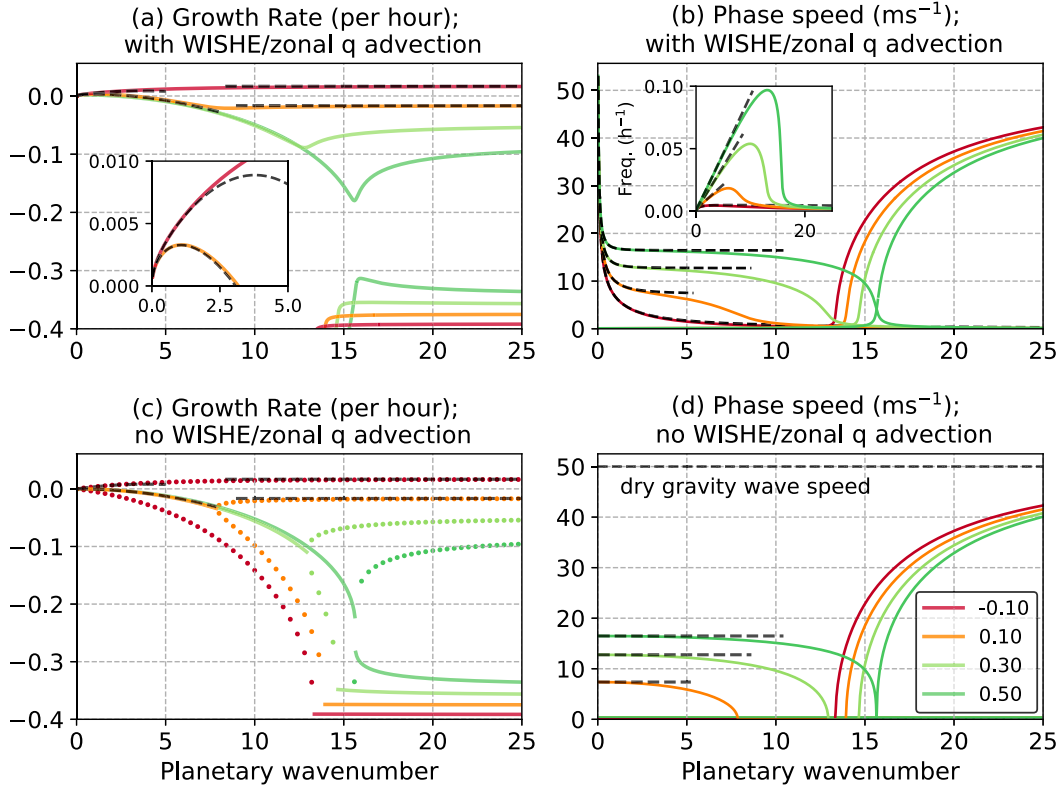


FIG. 3. Numerical solutions of the (left) growth rates and (right) phase speeds for valid modes of the $v = 0$ system (a),(b) with and (c),(d) without WISHE/zonal moisture advection. The colored lines indicate different values of the effective gross moist stability m_{eff} . The black dashed lines in (a) and (c) are analytic approximations in the longwave regime from (26) and the shortwave regime from (40)—for $m_{\text{eff}} = 0.1$ and $m_{\text{eff}} = -0.1$. The inset in (a) zooms in closer to the longwave regime. The black dashed lines in (b) and (d) are the analytic approximations to the phase speed in the longwave limit. The inset figure in (b) shows the frequency of the slowly propagating mode as a function of wavenumber. The dotted lines in (c) denote the stationary solutions.

this bifurcation happens at $k_p \sim 7$, where the two dotted orange stationary solutions meet the solid orange propagating solution. For $m_{\text{eff}} < 0$ the solution branches remain continuous. However, knowledge of where this bifurcation occurs for $m_{\text{eff}} > 0$ can give insight into the wavenumber of QE–WTG transition for other cases.

The phase speeds in Fig. 3d also clearly display the cutoff wavenumber for gravity wave emergence, as in Fig. 3b. The location of this cutoff wavenumber appears to coincide with a secondary bifurcation in Fig. 3c, where two stationary solutions merge into a propagating solution. Note that only one of these stationary solutions is shown in Fig. 3c; the other stationary solution can be seen in Fig. S3 of the online supplemental material. From Fig. 3d, it is also seen that the QE modes no longer display the singularity at $k = 0$ in the absence of WISHE/zonal moisture advection and are instead nondispersive with phase speeds near the longwave limit given by $c(m_r)^{1/2}$.

Two transition wavenumbers were identified from the numerical solutions in Fig. 3. The first of these marks the QE–WTG transition. The second wavenumber is associated with the transition between the slowly propagating mode in (27) and

the gravity waves in (39). In the solutions without WISHE/zonal moisture advection (Fig. 3c) and with $m_{\text{eff}} > 0$, both these transitions are marked by bifurcations between propagating and stationary solutions, making the transition in behavior particularly clear. The schematic in Fig. 4 isolates the dispersion curve for $m_{\text{eff}} = 0.1$ and summarizes key features of the QE–WTG transition and gravity wave emergence for cases with and without WISHE/zonal moisture advection. The smooth transitions in the former case are related to the bifurcations in the latter. In this figure, the wavenumbers that mark the QE–WTG transition and the emergence of gravity waves are termed k_{QW} and k_g , respectively. In the $v = 0$ model, the wavenumbers k_{QW} and k_g can be interpreted as upper bounds for the spatial scales of moisture modes and gravity waves, respectively. A detailed analysis of the factors affecting k_{QW} and k_g is pursued in section 5.

b. Moisture–temperature ratios

The numerically computed roots of (20) are plugged into (19) to numerically evaluate γ_{qT} values. Figure 5 compares the absolute value of the computed γ_{qT} for the QE mode and the WTG moisture mode. Solutions are presented for cases both

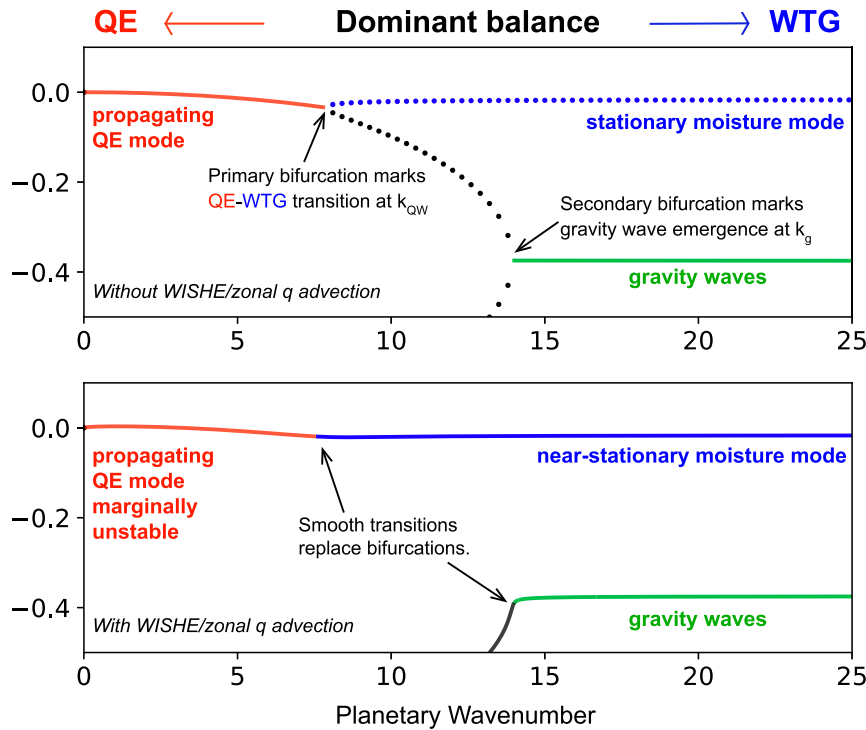


FIG. 4. A schematic summarizing the regimes and transitions in the $v = 0$ model for fixed $m_{\text{eff}} = 0.1$. The y axes indicate the growth rates. Shown are solutions in the (top) absence and (bottom) presence of WISHE/zonal moisture advection. The solid lines denote propagating solutions, and the dotted lines denote stationary solutions. Two bifurcations between stationary and propagating solutions are present in the top panel. The first of these bifurcations marks the transition wavenumber between the QE mode (red) and the WTG moisture mode (blue). The second bifurcation marks the emergence of gravity/short Kelvin waves damped by convection (green). The corresponding transitions persist in the WISHE/zonal-moisture-advection case but are smooth.

with and without WISHE/zonal moisture advection. For small wavenumbers, $|\gamma_{qT}| \sim \gamma_{QE}$, as predicted by the q - T ratio expression for the QE mode in (33). As the wavenumber is increased, $|\gamma_{qT}|$ grows rapidly; the rate of growth is quadratic, as predicted by the q - T ratio expression for the WTG mode in (41). The magnitudes of $|\gamma_{qT}|$ clearly highlight the distinction between longwave QE modes and the shortwave WTG moisture modes as depicted in Fig. 4. The QE mode can have a large humidity signature—with γ_{qT} slightly greater than γ_{QE} for precipitation to occur—but also has a nonnegligible temperature signal. The WTG moisture mode, on the other hand, has a humidity signature that dominates temperature by more than an order of magnitude.

When $m_{\text{eff}} < 0$, $|\gamma_{qT}|$ commences its departure from γ_{QE} at $k_p = 0$. When $m_{\text{eff}} > 0$, the departures of $|\gamma_{qT}|$ from γ_{QE} begin at positive wavenumbers that increase with m_{eff} . For instance, when $m_{\text{eff}} = 0.3$ and $m_{\text{eff}} = 0.5$, $|\gamma_{qT}|$ increases away from γ_{QE} for $k_p \sim 12$ and $k_p \sim 15$, respectively. The transition appears smoother when $m_{\text{eff}} = 0.1$, with $|\gamma_{qT}|$ increasing gradually away from γ_{QE} for $k_p \lesssim 7$ and then increasing rapidly beyond $k_p \sim 7$. These wavenumbers that mark the rapid increase in $|\gamma_{qT}|$ appear to coincide with the QE–WTG transition wavenumber inferred from Figs. 3a and 3c.

The presence of WISHE/zonal moisture advection only has a quantitative effect on $|\gamma_{qT}|$. For instance, when $m_{\text{eff}} = 0.1$, the departures from γ_{QE} grow faster in the presence of WISHE/zonal moisture advection than without. In the

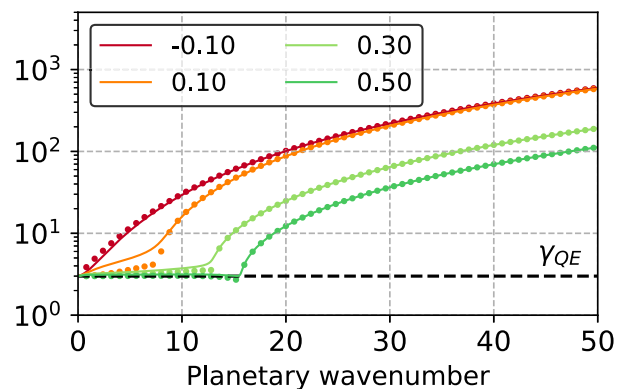


FIG. 5. Absolute values of the q - T ratio for the QE mode and WTG moisture mode with (solid lines) and without (dotted lines) WISHE/zonal moisture advection. The strict QE ratio γ_{QE} is indicated by the dashed horizontal line. The colors denote different values of m_{eff} .

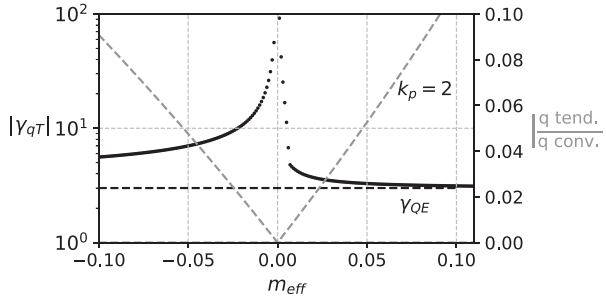


FIG. 6. Left axis: absolute values of γ_{qT} (dots) for small magnitudes of m_{eff} and planetary wavenumber fixed at $k_p = 2$. Right axis: the corresponding ratio between moisture tendency and moisture convergence (dashed line). The horizontal dashed black line denotes γ_{QE} for the left axis.

presence of WISHE/zonal moisture advection, $|\gamma_{qT}|$ increases along a continuous curve that leads from the QE mode to the WTG moisture mode. In the absence of WISHE/zonal moisture advection, there can be a discontinuity in the slope of $|\gamma_{qT}|$ as a function of k due to the primary bifurcation that marks the QE–WTG transition, as pointed out in Figs. 3c and 4.

Figure 6 shows how $|\gamma_{qT}|$ for the small m_{eff} moisture mode represented by (48) varies as m_{eff} approaches 0, with wavenumber fixed at $k_p = 2$. The absolute value of the ratio between the moisture tendency and moisture convergence computed from (44) is also displayed. The $|\gamma_{qT}|$ values increase rapidly as $m_{\text{eff}} \rightarrow 0$ from both positive and negative directions, with a singularity at $m_{\text{eff}} = 0$. These large values of $|\gamma_{qT}|$ are consistent with the expectations from the analytic solutions that this mode satisfies C2. Figure 6 also highlights the sensitive nature of the mode to perturbations in m_{eff} : as m_{eff} departs from zero, the $|\gamma_{qT}|$ ratios rapidly decrease to much smaller values closer to γ_{QE} . On the positive- m_{eff} side, the zone with large $|\gamma_{qT}|$ is very narrow, roughly $m_{\text{eff}} < 0.01$. The magnitude of moisture tendency relative to moisture convergence also diminishes with decreasing m_{eff} and vanishes at $m_{\text{eff}} = 0$.

5. The QE–WTG transition and gravity wave emergence

In this section, we will examine the factors that control the transition between QE and WTG (at $k = k_{\text{QW}}$) and the emergence of gravity waves (at $k = k_g$). For positive m_{eff} and without WISHE, k_{QW} and k_g coincide with bifurcations pointed out in Fig. 4, so they can be identified by locating these bifurcation wavenumbers. The physical balances found this way can then be used to inform extension to negative m_{eff} or WISHE cases. To this end, we first inspect the discriminant of the cubic equation in (20). For solutions without WISHE/zonal moisture advection, i.e., $\sigma_x = 0$, the cubic discriminant is

$$\Delta = 4c^4k^4 - \varepsilon_a^2(1 + 18m_r - 27m_r^2)c^2k^2 + 4\varepsilon_a^4m_r. \quad (49)$$

The bifurcations occur when Δ passes through zero, so the roots of $\Delta = 0$ should yield k_{QW} and k_g . Since (49) is quadratic in c^2k^2 , we can solve for the zeros of Δ to get

$$k^2 = \frac{\varepsilon_a^2}{8c^2}(1 + 18m_r - 27m_r^2) \left[1 \pm \sqrt{1 - \frac{64m_r}{(1 + 18m_r - 27m_r^2)^2}} \right]. \quad (50)$$

Solutions to (50) that yield real k give the transition wavenumbers. When m_r (or m_{eff}) is small, the term inside the square root in (50) is close to 1, so we have

$$k_{\text{QW}} \approx \frac{2\varepsilon_a}{c}\sqrt{m_r} = 2\frac{\sqrt{\varepsilon_a\varepsilon_q}}{c}\sqrt{m_{\text{eff}}} \quad \text{and} \quad (51)$$

$$k_g \approx \frac{\varepsilon_a}{2c}, \quad (52)$$

for $m_{\text{eff}} > 0$. When m_{eff} is close to 0, the QE–WTG transition occurs for small k_p , as seen from (51), but increases rapidly as $(m_{\text{eff}})^{1/2}$, reaching $k_p = 8$ near $m_{\text{eff}} = 0.1$. Gravity waves only emerge for modes with wavenumbers larger than the threshold wavenumber given in (52), which is a simple combination ε_a and c . This formulation in (52) is consistent with the threshold wavenumber inferred for the mode λ_5 in (47), which separates convectively adjusted modes from gravity wave adjusted modes in the limit of small m_{eff} . The formula (52) also gives insight into the bifurcations of multiple gravity wave branches (YN94) when more vertical degrees of freedom are included—the dry phase speeds associated with different vertical modes yield different values of k_g . In Fig. 4, the transitions are displayed for $m_{\text{eff}} = 0.1$, so $k_{\text{QW}} \sim 8$ using (51), and $k_g \sim 14$ using (52).

As m_r increases, it reaches a value where these two roots (k_g and k_{QW}) merge. This occurs where the term inside the square root in (50) is 0 at $m_r = 1/9$:

$$k_{\text{QW}} = k_g = \frac{\varepsilon_a}{\sqrt{3}c}; \quad (53)$$

that is, the merger occurs at approximately $m_{\text{eff}} = 0.51$ and $k_p \sim 16$ for values in Table 1. The approximate expression (51) for k_{QW} has only $\sim 14\%$ error at the merger point.

A physical interpretation of these analytic results is that the competition between the time scales for convective adjustment (ε_a) and gravity/Kelvin wave adjustment (ck) governs both the small length scales for QE modes and large length scales for gravity waves. This competition sets the scale of the gravity wave transition near where the ratio of the convective adjustment time scale ε_a and gravity wave frequency ck is order 1. For the QE mode and the moisture mode, the interaction is further moderated by m_{eff} , which can be viewed on the one hand as a reduction in dry static stability by convective heating (Emanuel et al. 1994), and on the other as the efficiency with which convection dries the column (Inoue and Back 2017). Small values of m_{eff} reduce the efficacy of convective adjustment, as seen in the moisture mode decay rate, and reduce the QE mode propagation speed. This competition results in the QE–WTG transition near where the ratio of the moisture adjustment time scale $\varepsilon_q m_{\text{eff}}$ and the QE mode frequency $(\varepsilon_q m_{\text{eff}}/\varepsilon_a)^{1/2} ck$ is order 1. Similar balances hold in the case of negative m_{eff} for the QE mode growth rate.

Figure 7 shows k_{QW} and k_g directly computed using (50) for the range of m_{eff} values over which real roots occur. The rapid change of the QE–WTG transition k_{QW} as m_{eff} increases from

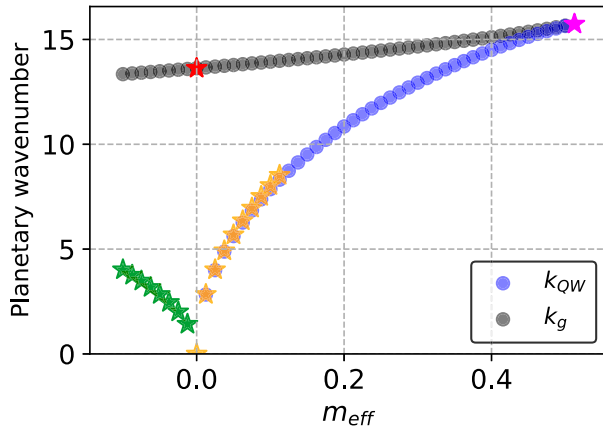


FIG. 7. Planetary wavenumbers for QE–WTG transition (k_{OW} ; blue dots) and gravity wave emergence (k_g ; gray dots) as a function of m_{eff} . The star markers denote the different approximate solutions to k_{OW} and k_g . The red star marks the approximate k_g value at small m_{eff} computed using (52). The orange stars mark approximate k_{OW} values for $m_{eff} \geq 0$ computed using (51), and the green stars are the approximate k_{OW} values for $m_{eff} < 0$ computed using (54). The magenta star denotes the k_g and k_{OW} values at the merger point, computed using (53).

zero is well approximated by (51). The gravity wave transition k_g increases less rapidly with m_{eff} , as expected since the gravity wave dynamics is less dependent on the moist stability. The case $m_{eff} = 0.5$ in Figs. 3c and 3d shows the behavior where the QE–WTG transition has almost reached the merger with the gravity wave transition, corresponding to m_{eff} just slightly less than the value marked by the cyan star in Fig. 7. With increased m_{eff} , the WTG mode decay rate has increased such that the dip at the QE–WTG merger cusp is close to the decay rate of the gravity waves, and the region with no propagating mode between the two transitions has become very small. For $m_{eff} > 0.51$, the QE mode transitions continuously to the gravity wave branch and the moisture mode decay rate changes rapidly near $k = \varepsilon_a/(3^{1/2}c)$ to connect to a strongly damped mode at low wavenumbers (Fig. S3 of the online supplemental material).

The bifurcations identified by $\Delta = 0$ in (50) move off the real k axis when $\sigma_x \neq 0$, so there are no longer singular mergers with degenerate eigenvalues at particular real k values and—as shown in Fig. 4—the QE and WTG eigenvalues lie on the same solution branch. However, closely related behavior with similar physical balances still arises in some neighborhood of the $\sigma_x = 0$ bifurcations. This may be seen in the correspondence between slightly smoothed extrema of growth rates in Fig. 3a and the location of bifurcations in Fig. 3c, and in the similarities in phase speed transitions between Figs. 3b and 3d.

When $m_{eff} < 0$, changes in regime are not marked by dramatic bifurcations. However, the changes in dominant balances similar to the $m_{eff} > 0$ case still occur as a function of k . To identify a characteristic k scale where the QE–WTG crossover occurs for $m_{eff} < 0$, we can seek an approximate match between small- k approximation for the QE mode (26) and the large- k approximation for the WTG moisture mode

(40). To leading order (26) gives $\lambda = ck(\varepsilon_q/\varepsilon_a)^{1/2}|m_{eff}|^{1/2}$ and (40) gives $\lambda = \varepsilon_q|m_{eff}|$. Equating these yields

$$k_{OW} = \frac{\sqrt{\varepsilon_q \varepsilon_a}}{c} \sqrt{|m_{eff}|}. \quad (54)$$

This has the same scale and m_{eff} dependence as (51) in the positive m_{eff} case, but is smaller by a factor of $1/2$. In Fig. 7, this is seen as an asymmetry in the k_{OW} transition for positive and negative m_{eff} ; in contrast, k_g crosses smoothly to negative m_{eff} . The approximation (54) is also consistent with the $m_{eff} = -0.1$ case in Figs. 3a and 3c, which suggests that the analytic expression for the moisture mode is not valid until $k_p \sim 7$.

For this $m_{eff} < 0$ case, one can also ask for what wavenumber the q – T ratio becomes much larger than γ_{QE} , a signature of the moisture mode as outlined in C1. Using the leading-order term from (26) in (19), and $m_r \ll 1$ yields:

$$k \gg \frac{\varepsilon_t}{c} (1+r) \sqrt{\frac{\varepsilon_q}{\varepsilon_a}} \sqrt{|m_{eff}|}. \quad (55)$$

This has the same m_{eff} dependence as (54); the scaling factor is similar but with $\varepsilon_t(1+r)$ in place of ε_a , so it is smaller by a factor of 0.78 for standard parameters.

Previous studies (Fuchs and Raymond 2002, 2005) have documented the gravity wave emergence, but noted that this emergence occurs at unrealistically long wavelengths, larger than Earth’s circumference ($k_p < 1$). This result can be explained by considering the expression for k_g in (52) for different values of ε_a . For the parameter values in Table 1, $\varepsilon_a^{-1} = 1.3$ h, which yields $k_g \sim 13.6$. Fuchs and Raymond (2002, 2005) employ a longer convective adjustment time scale ~ 1 day. Using $\varepsilon_a^{-1} = 24$ h in (52) yields $k_g \sim 0.7$, which is indeed an unrealistically large length scale for gravity waves. The wavenumber of gravity wave emergence is therefore sensitive to the choice of convective adjustment time scale.

6. The $v \neq 0$ case

A complete treatment of the $v \neq 0$ case can be pursued by deriving the dispersion relationship from the governing equations in (5)–(9). In this section, we only pursue the simply extendable properties from the $v = 0$ solutions to the $v \neq 0$ case. Specifically, we seek to verify if the QE and WTG balances characterize the longwave and shortwave regimes when $v \neq 0$, like they do in the $v = 0$ case. For this purpose, we only require the leading-order term in the solution to the dispersion relationship in the large- k and small- k regimes. For simplicity, we neglect WISHE/zonal moisture advection, i.e., set $\xi = 0$.

a. Long Rossby waves

Solutions to Equatorial Rossby waves in the small- k regime are analogous to the long Kelvin wave solutions—in (26)—through the equatorial longwave approximation (Gill 1982; Boyd 2018). At the leading order and after neglecting WISHE/zonal moisture advection, these modes have the following solutions:

$$\lambda_7 = \frac{ick}{2n+1}\sqrt{m_r} + O(k^2), \tag{56}$$

where n is a nonnegative integer. The moisture–temperature ratio for the long Rossby wave is obtained after using (56) in the expression for q – T ratio (19):

$$\gamma_{qT} = \gamma_{QE} - i\delta \frac{\sqrt{m_r} \varepsilon_a}{2n+1 \varepsilon_q} \left[\frac{(2n+1)^2 - m_r}{1+r} \right] + O(\delta^2). \tag{57}$$

From (57) it is evident that as $\delta \rightarrow 0$ and $\gamma_{qT} \rightarrow \gamma_{QE}$. The long Rossby waves, when coupled to convection, tend toward the QE balance like the long Kelvin waves. The convective heating for this mode is calculated by using (57) in the precipitation closure expression (18):

$$\hat{Q}_{Ro} = -i\varepsilon_a \hat{T} \frac{\sqrt{m_r}}{2n+1} \left[\frac{(2n+1)^2 - m_r}{1+r} \right] \delta + O(\delta^2). \tag{58}$$

From (56) and (58) it is evident that the tendency terms in the thermodynamic budgets (8) and (9) are of the same order: $O(k)$. To estimate the magnitude of the adiabatic cooling/moisture convergence term, it is sufficient to estimate the scale of the divergence. Following standard nondimensional procedures for the equatorial beta plane (Matsuno 1966), we scale y by the equatorial Rossby radius L_R :

$$y = y^* L_R = y^* \sqrt{c/\beta}, \tag{59}$$

where y^* is a nondimensional length scale. We also use c as the scale for the horizontal velocities:

$$(u_1, v_1) = (u^*c, v^*c). \tag{60}$$

With these scales, the leading-order balance in the divergence equation, (7), is

$$\omega_1 = ck \left(iu^* + \partial_y^* v^* \frac{1}{L_R k} \right). \tag{61}$$

For planetary scales, the coefficient of $\partial_y^* v^*$ is $O(1)$, so the divergence is of $O(k)$, and both the thermodynamic budgets retain full balances, similar to the budgets for the long Kelvin wave from (35) and (36). The convectively coupled long Rossby wave is therefore a QE mode.

b. Short Rossby waves

The primary governing equation for Rossby waves is the potential vorticity equation (Gill 1982), which we now use to extract the shortwave solutions. Equations (5) and (6) are first cast in vorticity–divergence form. The divergence is then eliminated by using (7) and (15) to get

$$\begin{aligned} & [\lambda^2(\lambda + \varepsilon_a) - (\lambda + m_{\text{eff}}\varepsilon_q)c^2\nabla^2](\lambda\zeta + \beta v_1) \\ & + \lambda(\lambda + \varepsilon_a)\beta^2 y^2 \zeta = 0, \end{aligned} \tag{62}$$

where ζ is the vorticity:

$$\zeta = ikv_1 - \partial_y u_1 = -\nabla^2 \psi, \tag{63}$$

with ψ being the streamfunction that characterizes the non-divergent flow. Similar to the quasigeostrophic approximation, we neglect divergent flow in the planetary vorticity advection term:

$$v_1 \beta \approx -ik\psi\beta, \tag{64}$$

but retain the effects of divergence in temperature and moisture equations where they are leading-order terms, so gravity waves still exist in this system. Inserting (63) and (64) in (62) yields the potential vorticity equation:

$$\begin{aligned} & \{[\lambda^2(\lambda + \varepsilon_a) - (\lambda + m_{\text{eff}}\varepsilon_q)c^2\nabla^2](\lambda\nabla^2 + ik\beta) \\ & + \lambda(\lambda + \varepsilon_a)\beta^2 y^2 \nabla^2\} \psi = 0. \end{aligned} \tag{65}$$

When considering motions with rapid zonal variations and spatially broad meridional structures, a perturbation expansion of (65) yields four roots—see the online supplemental material for a full derivation. The leading-order solutions are

$$\lambda_8 = -\varepsilon_q m_{\text{eff}}, \tag{66}$$

$$\lambda_9 = i\beta/k, \quad \text{and} \tag{67}$$

$$(\lambda_{10}, \lambda_{11}) = \pm ick - \frac{\varepsilon_q m_{\text{eff}}}{2} \left(\frac{1 - m_r}{m_r} \right). \tag{68}$$

It is sufficient to compare (66) with (40) and conclude that λ_8 is a WTG moisture mode. This mode has the same properties as its counterpart in the $v = 0$ model and satisfies conditions C1, C2, and C3. Since this mode is derived out of the $v \neq 0$ case, it will possess a different meridional structure than the $v = 0$ moisture mode. It is noteworthy that *the WTG moisture mode does not possess a unique meridional structure*. This result explains why the moisture mode solution of Adames and Kim (2016), which is a superposition of Kelvin and Rossby wave structures, is nearly identical to the dispersion relation for the shortwave $v = 0$ moisture mode in (40).

The solution in (67) is the shortwave limit of the dry Rossby wave (Matsuno 1966). It can be verified that γ_{qT} for this mode tends to γ_{QE} , such that it is nonprecipitating at the leading order. However, it should be noted that this mode will not play a prominent role in the thermodynamic adjustment process because it is not damped by convection at leading order. The two solutions in (68) are gravity waves that perform the fast adjustment on to the WTG line, like in Fig. 2.

The QE and WTG balances therefore characterize the long and short wave regimes even in the $v \neq 0$ model. The details of the QE–WTG transitions can, however, only be pursued with numerical solutions of the full dispersion relationship (e.g., Emanuel 1993; Fuchs and Raymond 2005; Fuchs-Stone et al. 2019; Emanuel 2020). These details are currently under examination and will feature in future work.

7. Summary and discussion

a. Summary

Analytic approximations are used to solve the dispersion relationship from an equatorial beta plane model with an

empirical precipitation closure under limiting regimes. These approximations are used to compute moisture–temperature ratios and illustrate the dominant balances that characterize the modes of the system. The empirical precipitation closure has different time scales associated with temperature versus moisture sensitivities. The ratio of these sensitivities (γ_{QE}) governs important properties of the model. The planetary-scale Kelvin and Rossby waves are primarily adjusted by convection, so they have leading-order moisture–temperature ratios close to γ_{QE} (some departure is required for precipitation to occur). These modes are accordingly characterized as QE modes. The phase speeds of these QE modes is also dependent on γ_{QE} , in addition to the effective gross moist stability. Gravity waves are absent in the longwave limit, and the fast adjustment in this limit instead occurs at the convective adjustment time scale. Three specific conditions are introduced to identify moisture modes and distinguish them from QE modes: a large moisture–temperature ratio ($\gamma_{qT} \gg \gamma_{QE}$), large prognostic moisture variations, and the loss of the temperature tendency term. Moisture modes primarily emerge at large wavenumbers because fast adjustment to WTG occurs by gravity waves; but they can extend to lower wavenumbers for near-zero values of the effective gross moist stability. The moisture modes can exist with both Kelvin and Rossby wave meridional structures. Ways to similarly identify moisture modes in observations are discussed in [section 7d](#).

Numerical solutions for the $v = 0$ case identify two wavenumber cutoffs: one that separates the QE and WTG moisture modes, and another above which gravity waves emerge in the system. For the solutions without WISHE/zonal moisture advection, these transitions are marked by bifurcations between stationary and propagating solution. The bifurcations are used to analytically estimate the wavenumber cutoffs, which turn out to be simple combinations of the convective adjustment time scale and the gravity wave speed. The inclusion of WISHE/zonal moisture advection alters the nature of the QE–WTG transition and emergence of gravity waves from abrupt bifurcations to smooth transitions.

b. Tropical wave speeds

The departure of the observed convectively coupled wave speeds from the dry wave speeds has two general sets of explanations: (i) a reduced gross moist stability ([Neelin and Held 1987](#); [Emanuel et al. 1994](#)) or (ii) multiple baroclinic modes ([Mapes 2000](#); [Majda and Shefter 2001](#); [Majda et al. 2004](#); [Khouider and Majda 2006, 2008](#); [Kuang 2008](#)). The analytic solutions in this study show that the wave speeds are also sensitive to details of the convective coupling. Even with a single baroclinic mode, introducing a different temperature dependence relative to the moisture dependence for precipitation alters the wave phase speeds by a factor that depends on γ_{QE} . With empirically informed values for γ_{QE} , the QE modes propagate at speeds substantially slower than implied by the gross moist stability alone, and much slower than the dry Matsuno modes. Differences in the moisture–temperature dependence of precipitation therefore supplies an alternate hypothesis for the slow observed phase speeds of convectively coupled waves.

c. Critical wavenumber for convective coupling

In this study, convectively coupled QE modes only exist for wavenumbers smaller than the QE–WTG transition wavenumber (k_{QW}), above which they transition to moisture modes. Gravity waves emerge only for wavenumbers greater than the wavenumber for gravity wave emergence (k_g). The values of k_{QW} and k_g are simple combinations of the convective adjustment time scale, the dry gravity wave speed and the effective gross moist stability. The apparent critical wavenumber for gravity wave emergence is also seen in models with higher-order vertical structures: e.g., see Fig. 3 in [YN94](#), Fig. 3 in [Khouider and Majda \(2006\)](#), and Fig. 4 in [Kuang \(2018\)](#), suggesting generality that extends beyond the $v = 0$ case with a single baroclinic mode. It is therefore worth considering if these wavenumber cutoffs have observational relevance. For a typical value of effective gross moist stability, the QE–WTG transition wavenumber occurs close to planetary wavenumber 8. In the observed intraseasonal power spectrum ([Wheeler and Kiladis 1999](#); [Kiladis et al. 2009](#)), the power corresponding to convectively coupled Kelvin waves does not extend beyond planetary wavenumber ~ 10 . The QE–WTG transition might therefore explain the smallest length scale up to which Kelvin waves are convectively coupled, i.e., where the dominant thermodynamic adjustment is due to convection and not gravity waves.

d. Moisture mode variety

The WTG moisture mode has been used as a prototype to study the planetary-scale MJO ([Sobel and Maloney 2012, 2013](#); [Adames and Kim 2016](#)). This study highlights that moisture modes are more prevalent at shorter length scales or under conditions in which $m_{\text{eff}} \rightarrow 0$. These modes also do not possess a fixed meridional structure, and can assume any form imposed by the dynamical constraints—both Kelvin wave and Rossby wave meridional structures in the case of this study. This would suggest that observational analogs of the moisture mode are likely to be found as shortwave, near-stationary modes with respect to the mean flow with large moisture–temperature ratios but that specific conditions would have to apply for the moisture mode to be a good analog to observed planetary scale variance. Two possibilities consistent with results here are considered in turn below.

Imposing the WTG approximation—tantamount to assuming an infinite gravity wave speed—will eliminate the QE mode and allow moisture modes to extend to planetary scales. For finite gravity wave speeds and nonzero m_{eff} values, pure WTG moisture modes cannot exist at planetary scales. However, there exist transition zones in which planetary-scale disturbances can exist as intermediate modes with properties of both QE and WTG moisture modes. In the $v = 0$ case, these intermediate modes are evocative of “mixed-moisture gravity waves” from [Adames et al. \(2019\)](#). The small gross moist stability regime is posited to exist within the MJO and long equatorial Rossby wave wavenumber–frequency bands ([Inoue et al. 2020](#); [Benedict et al. 2020](#)), suggesting that these disturbances are also likely to exist as intermediate modes between QE and WTG.

Moisture modes can extend to the planetary length scale if the gross moist stability approaches zero (although the range of validity of the small- m_{eff} moisture modes is limited to a narrow range of m_{eff} values). It is suggested that planetary scale disturbances that satisfy the WTG temperature balance (e.g., Wolding et al. 2016) are likely to be small- m_{eff} moisture modes. In the idealized modeling world, the phenomenon of convective self-aggregation (Bretherton et al. 2005; Muller and Held 2012; Wing and Emanuel 2014; Wing et al. 2018) can also be viewed as a moisture mode (as recognized in Sugiyama 2009; Raymond and Fuchs 2009; Kuang 2018). The strongly feedback-dominated nature of self-aggregated clusters (Ahmed and Neelin 2019) suggests that this mode likely exists in the small or negative gross moist stability regimes.

Observed tropical intraseasonal disturbances—including equatorial waves, African easterly waves, and monsoon low-pressure systems—can be placed the QE–WTG continuum by verifying how they satisfy conditions C1–C3. Such an exercise would help address questions surrounding the moisture mode character of disturbances such as the MJO (Fuchs and Raymond 2017; Adames et al. 2019). For instance, an initial examination (not shown) of the q – T ratio for the MJO using regression analysis—as in Ahmed and Schumacher (2018)—yields values ~ 5 – 6 . Though this result is preliminary, it suggests that the MJO lies in the transition zone between QE and moisture modes. A more thorough examination would isolate the different vertical structures in these disturbances, display the ratios in wavenumber–frequency space and account for phase shifts between temperature and moisture perturbations (e.g., as in Yasunaga et al. 2019; Inoue et al. 2020). These examinations will be considered in a future observational study.

e. Connections to models with higher-order vertical structures

It is worth commenting on whether the results from this study are extendable to related models with different treatments for vertical structures. This treatment can either include two baroclinic modes for the convective heating (Mapes 2000; Majda and Shefter 2001; Majda et al. 2004; Khouider and Majda 2006, 2008; Kuang 2008; Andersen and Kuang 2008; Stechmann and Hottovy 2017) or a single baroclinic mode with radiation upper-boundary conditions (Yano and Emanuel 1991; Raymond and Fuchs 2007; Fuchs et al. 2012). Stationary moisture modes appear to exist in both classes of models (Khouider and Majda 2006; Raymond and Fuchs 2007, 2009; Kuang 2018). A wavenumber-dependent transition to QE at small wavenumbers can occur under convective adjustment (YN94) but whether or how it extends to other parameterizations within these solutions is worth examining. These models also contain solutions not found with the use of a single baroclinic mode: unstable, convectively coupled Kelvin waves that extend to planetary scales in a few cases (e.g., Khouider and Majda 2006; Fuchs and Raymond 2007; Raymond and Fuchs 2007), but not in others (Kuang 2018). It would be interesting to examine the dominant balances and wavenumber-dependent transitions in these solutions. This set of questions can be

addressed within the framework of this study by incorporating higher-order vertical structures in the governing equations.

Acknowledgments. This research was supported by National Science Foundation Grants AGS-1936810 (authors Ahmed and Neelin) and AGS-1841559 (author Adames).

REFERENCES

- Adames, Á. F., and D. Kim, 2016: The MJO as a dispersive, convectively coupled moisture wave: Theory and observations. *J. Atmos. Sci.*, **73**, 913–941, <https://doi.org/10.1175/JAS-D-15-0170.1>.
- , —, S. K. Clark, Y. Ming, and K. Inoue, 2019: Scale analysis of moist thermodynamics in a simple model and the relationship between moisture modes and gravity waves. *J. Atmos. Sci.*, **76**, 3863–3881, <https://doi.org/10.1175/JAS-D-19-0121.1>.
- Ahmed, F., and C. Schumacher, 2015: Convective and stratiform components of the precipitation–moisture relationship. *Geophys. Res. Lett.*, **42**, 10–453, <https://doi.org/10.1002/2015GL066957>.
- , and J. D. Neelin, 2018: Reverse engineering the tropical precipitation–buoyancy relationship. *J. Atmos. Sci.*, **75**, 1587–1608, <https://doi.org/10.1175/JAS-D-17-0333.1>.
- , and C. Schumacher, 2018: Spectral signatures of moisture–convection feedbacks over the Indian Ocean. *J. Atmos. Sci.*, **75**, 1995–2015, <https://doi.org/10.1175/JAS-D-17-0138.1>.
- , and J. D. Neelin, 2019: Explaining scales and statistics of tropical precipitation clusters with a stochastic model. *J. Atmos. Sci.*, **76**, 3063–3087, <https://doi.org/10.1175/JAS-D-18-0368.1>.
- , Á. F. Adames, and J. D. Neelin, 2020: Deep convective adjustment of temperature and moisture. *J. Atmos. Sci.*, **77**, 2163–2186, <https://doi.org/10.1175/JAS-D-19-0227.1>.
- Andersen, J. A., and Z. Kuang, 2008: A toy model of the instability in the equatorially trapped convectively coupled waves on the equatorial beta plane. *J. Atmos. Sci.*, **65**, 3736–3757, <https://doi.org/10.1175/2008JAS2776.1>.
- Arakawa, A., and W. H. Schubert, 1974: Interaction of a cumulus cloud ensemble with the large-scale environment, Part I. *J. Atmos. Sci.*, **31**, 674–701, [https://doi.org/10.1175/1520-0469\(1974\)031<0674:IOACCE>2.0.CO;2](https://doi.org/10.1175/1520-0469(1974)031<0674:IOACCE>2.0.CO;2).
- Benedict, J. J., B. Medeiros, A. C. Clement, and J. G. Olson, 2020: Investigating the role of cloud–radiation interactions in subseasonal tropical disturbances. *Geophys. Res. Lett.*, **47**, e2019GL086817, <https://doi.org/10.1029/2019GL086817>.
- Betts, A. K., 1986: A new convective adjustment scheme. Part I: Observational and theoretical basis. *Quart. J. Roy. Meteor. Soc.*, **112**, 677–691, <https://doi.org/10.1002/qj.49711247307>.
- , and M. J. Miller, 1986: A new convective adjustment scheme. Part II: Single column tests using GATE wave, BOMEX, ATEX and arctic air-mass data sets. *Quart. J. Roy. Meteor. Soc.*, **112**, 693–709, <https://doi.org/10.1002/qj.49711247308>.
- Boyd, J. P., 2018: *Dynamics of the Equatorial Ocean*. Springer, 517 pp.
- Bretherton, C. S., M. E. Peters, and L. E. Back, 2004: Relationships between water vapor path and precipitation over the tropical oceans. *J. Climate*, **17**, 1517–1528, [https://doi.org/10.1175/1520-0442\(2004\)017<1517:RBWVPA>2.0.CO;2](https://doi.org/10.1175/1520-0442(2004)017<1517:RBWVPA>2.0.CO;2).
- , P. N. Blossey, and M. Khairoutdinov, 2005: An energy–balance analysis of deep convective self-aggregation above uniform SST. *J. Atmos. Sci.*, **62**, 4273–4292, <https://doi.org/10.1175/JAS3614.1>.
- Emanuel, K. A., 1987: An air–sea interaction model of intraseasonal oscillations in the tropics. *J. Atmos. Sci.*, **44**, 2324–2340, [https://doi.org/10.1175/1520-0469\(1987\)044<2324:AASIMO>2.0.CO;2](https://doi.org/10.1175/1520-0469(1987)044<2324:AASIMO>2.0.CO;2).

- , 1993: The effect of convective response time on WISHE modes. *J. Atmos. Sci.*, **50**, 1763–1776, [https://doi.org/10.1175/1520-0469\(1993\)050<1763:TEOCRT>2.0.CO;2](https://doi.org/10.1175/1520-0469(1993)050<1763:TEOCRT>2.0.CO;2).
- , 2020: Slow modes of the equatorial waveguide. *J. Atmos. Sci.*, **77**, 1575–1582, <https://doi.org/10.1175/JAS-D-19-0281.1>.
- , J. D. Neelin, and C. S. Bretherton, 1994: On large-scale circulations in convecting atmospheres. *Quart. J. Roy. Meteor. Soc.*, **120**, 1111–1143, <https://doi.org/10.1002/qj.49712051902>.
- Frierson, D. M. W., 2007: Convectively coupled Kelvin waves in an idealized moist general circulation model. *J. Atmos. Sci.*, **64**, 2076–2090, <https://doi.org/10.1175/JAS3945.1>.
- Fuchs, Ž., and D. J. Raymond, 2002: Large-scale modes of a non-rotating atmosphere with water vapor and cloud–radiation feedbacks. *J. Atmos. Sci.*, **59**, 1669–1679, [https://doi.org/10.1175/1520-0469\(2002\)059<1669:LSMOAN>2.0.CO;2](https://doi.org/10.1175/1520-0469(2002)059<1669:LSMOAN>2.0.CO;2).
- , and —, 2005: Large-scale modes in a rotating atmosphere with radiative–convective instability and WISHE. *J. Atmos. Sci.*, **62**, 4084–4094, <https://doi.org/10.1175/JAS3582.1>.
- , and —, 2007: A simple, vertically resolved model of tropical disturbances with a humidity closure. *Tellus*, **59A**, 344–354, <https://doi.org/10.1111/j.1600-0870.2007.00230.x>.
- , and —, 2017: A simple model of intraseasonal oscillations. *J. Adv. Model. Earth Syst.*, **9**, 1195–1211, <https://doi.org/10.1002/2017MS000963>.
- , S. Gjorgjievska, and D. J. Raymond, 2012: Effects of varying the shape of the convective heating profile on convectively coupled gravity waves and moisture modes. *J. Atmos. Sci.*, **69**, 2505–2519, <https://doi.org/10.1175/JAS-D-11-0308.1>.
- Fuchs-Stone, Ž., D. J. Raymond, and S. Sentić, 2019: A simple model of convectively coupled equatorial Rossby waves. *J. Adv. Model. Earth Syst.*, **11**, 173–184, <https://doi.org/10.1029/2018MS001433>.
- Gill, A. E., 1982: The tropics. *Atmosphere–Ocean Dynamics*, A. E. Gill, Ed., International Geophysics, Vol. 30, Academic Press, 429–491.
- Holton, J. R., and R. S. Lindzen, 1968: A note on Kelvin waves in the atmosphere. *Mon. Wea. Rev.*, **96**, 385–386, [https://doi.org/10.1175/1520-0493\(1968\)096<0385:ANOKWI>2.0.CO;2](https://doi.org/10.1175/1520-0493(1968)096<0385:ANOKWI>2.0.CO;2).
- Huffman, G. J., and Coauthors, 2007: The TRMM Multisatellite Precipitation Analysis (TMPA): Quasi-global, multiyear, combined-sensor precipitation estimates at fine scales. *J. Hydrometeorol.*, **8**, 38–55, <https://doi.org/10.1175/JHM560.1>.
- Inoue, K., and L. E. Back, 2017: Gross moist stability analysis: Assessment of satellite-based products in the GMS plane. *J. Atmos. Sci.*, **74**, 1819–1837, <https://doi.org/10.1175/JAS-D-16-0218.1>.
- , Á. F. Adames, and K. Yasunaga, 2020: Vertical velocity profiles in convectively coupled equatorial waves and MJO: New diagnoses of vertical velocity profiles in the wavenumber–frequency domain. *J. Atmos. Sci.*, **77**, 2139–2162, <https://doi.org/10.1175/JAS-D-19-0209.1>.
- Khouider, B., and A. J. Majda, 2006: A simple multicloud parameterization for convectively coupled tropical waves. Part I: Linear analysis. *J. Atmos. Sci.*, **63**, 1308–1323, <https://doi.org/10.1175/JAS3677.1>.
- , and —, 2008: Multicloud models for organized tropical convection: Enhanced congestus heating. *J. Atmos. Sci.*, **65**, 895–914, <https://doi.org/10.1175/2007JAS2408.1>.
- , and E. Leclerc, 2019: Toward a stochastic relaxation for the quasi-equilibrium theory of cumulus parameterization: Multicloud instability, multiple equilibria, and chaotic dynamics. *J. Adv. Model. Earth Syst.*, **11**, 2474–2502, <https://doi.org/10.1029/2019MS001627>.
- Kiladis, G. N., M. C. Wheeler, P. T. Haertel, K. H. Straub, and P. E. Roundy, 2009: Convectively coupled equatorial waves. *Rev. Geophys.*, **47**, RG2003, <https://doi.org/10.1029/2008RG000266>.
- Kim, D., M.-S. Ahn, I.-S. Kang, and A. D. Del Genio, 2015: Role of longwave cloud–radiation feedback in the simulation of the Madden–Julian oscillation. *J. Climate*, **28**, 6979–6994, <https://doi.org/10.1175/JCLI-D-14-00767.1>.
- Kuang, Z., 2008: A moisture-stratiform instability for convectively coupled waves. *J. Atmos. Sci.*, **65**, 834–854, <https://doi.org/10.1175/2007JAS2444.1>.
- , 2018: Linear stability of moist convecting atmospheres. Part I: From linear response functions to a simple model and applications to convectively coupled waves. *J. Atmos. Sci.*, **75**, 2889–2907, <https://doi.org/10.1175/JAS-D-18-0092.1>.
- Kuo, Y.-H., K. A. Schiro, and J. D. Neelin, 2018: Convective transition statistics over tropical oceans for climate model diagnostics: Observational baseline. *J. Atmos. Sci.*, **75**, 1553–1570, <https://doi.org/10.1175/JAS-D-17-0287.1>.
- Lin, J.-L., and B. E. Mapes, 2004: Radiation budget of the tropical intraseasonal oscillation. *J. Atmos. Sci.*, **61**, 2050–2062, [https://doi.org/10.1175/1520-0469\(2004\)061<2050:RBOTTI>2.0.CO;2](https://doi.org/10.1175/1520-0469(2004)061<2050:RBOTTI>2.0.CO;2).
- , T. Qian, T. Shinoda, and S. Li, 2015: Is the tropical atmosphere in convective quasi-equilibrium? *J. Climate*, **28**, 4357–4372, <https://doi.org/10.1175/JCLI-D-14-00681.1>.
- Madden, R. A., and P. R. Julian, 1971: Detection of a 40–50-day oscillation in the zonal wind in the tropical Pacific. *J. Atmos. Sci.*, **28**, 702–708, [https://doi.org/10.1175/1520-0469\(1971\)028<0702:DOADOI>2.0.CO;2](https://doi.org/10.1175/1520-0469(1971)028<0702:DOADOI>2.0.CO;2).
- , and —, 1994: Observations of the 40–50-day tropical oscillation—A review. *Mon. Wea. Rev.*, **122**, 814–837, [https://doi.org/10.1175/1520-0493\(1994\)122<0814:OOTDTO>2.0.CO;2](https://doi.org/10.1175/1520-0493(1994)122<0814:OOTDTO>2.0.CO;2).
- Majda, A. J., and M. G. Shefter, 2001: Models for stratiform instability and convectively coupled waves. *J. Atmos. Sci.*, **58**, 1567–1584, [https://doi.org/10.1175/1520-0469\(2001\)058<1567:MFSIAC>2.0.CO;2](https://doi.org/10.1175/1520-0469(2001)058<1567:MFSIAC>2.0.CO;2).
- , B. Khouider, G. N. Kiladis, K. H. Straub, and M. G. Shefter, 2004: A model for convectively coupled tropical waves: Nonlinearity, rotation, and comparison with observations. *J. Atmos. Sci.*, **61**, 2188–2205, [https://doi.org/10.1175/1520-0469\(2004\)061<2188:AMFCCT>2.0.CO;2](https://doi.org/10.1175/1520-0469(2004)061<2188:AMFCCT>2.0.CO;2).
- Mapes, B. E., 2000: Convective inhibition, subgrid-scale triggering energy, and stratiform instability in a toy tropical wave model. *J. Atmos. Sci.*, **57**, 1515–1535, [https://doi.org/10.1175/1520-0469\(2000\)057<1515:CISSTE>2.0.CO;2](https://doi.org/10.1175/1520-0469(2000)057<1515:CISSTE>2.0.CO;2).
- Matsuno, T., 1966: Quasi-geostrophic motions in the equatorial area. *J. Meteor. Soc. Japan*, **44**, 25–43, https://doi.org/10.2151/jmsj1965.44.1_25.
- Muller, C. J., and I. M. Held, 2012: Detailed investigation of the self-aggregation of convection in cloud-resolving simulations. *J. Atmos. Sci.*, **69**, 2551–2565, <https://doi.org/10.1175/JAS-D-11-0257.1>.
- Neelin, J. D., and I. M. Held, 1987: Modeling tropical convergence based on the moist static energy budget. *Mon. Wea. Rev.*, **115**, 3–12, [https://doi.org/10.1175/1520-0493\(1987\)115<0003:MTCBOT>2.0.CO;2](https://doi.org/10.1175/1520-0493(1987)115<0003:MTCBOT>2.0.CO;2).
- , and J.-Y. Yu, 1994: Modes of tropical variability under convective adjustment and the Madden–Julian oscillation. Part I: Analytical theory. *J. Atmos. Sci.*, **51**, 1876–1894, [https://doi.org/10.1175/1520-0469\(1994\)051<1876:MOTVUC>2.0.CO;2](https://doi.org/10.1175/1520-0469(1994)051<1876:MOTVUC>2.0.CO;2).
- , and N. Zeng, 2000: A quasi-equilibrium tropical circulation model—formulation. *J. Atmos. Sci.*, **57**, 1741–1766, [https://doi.org/10.1175/1520-0469\(2000\)057<1741:AQETCM>2.0.CO;2](https://doi.org/10.1175/1520-0469(2000)057<1741:AQETCM>2.0.CO;2).

- , I. M. Held, and K. H. Cook, 1987: Evaporation-wind feedback and low-frequency variability in the tropical atmosphere. *J. Atmos. Sci.*, **44**, 2341–2348, [https://doi.org/10.1175/1520-0469\(1987\)044<2341:EWFALF>2.0.CO;2](https://doi.org/10.1175/1520-0469(1987)044<2341:EWFALF>2.0.CO;2).
- , O. Peters, J. W.-B. Lin, K. Hales, and C. E. Holloway, 2008: Rethinking convective quasi-equilibrium: Observational constraints for stochastic convective schemes in climate models. *Philos. Trans. Roy. Soc.*, **366A**, 2581–2604, <https://doi.org/10.1098/rsta.2008.0056>.
- , —, and K. Hales, 2009: The transition to strong convection. *J. Atmos. Sci.*, **66**, 2367–2384, <https://doi.org/10.1175/2009JAS2962.1>.
- Peters, O., and J. D. Neelin, 2006: Critical phenomena in atmospheric precipitation. *Nat. Phys.*, **2**, 393–396, <https://doi.org/10.1038/nphys314>.
- Raymond, D. J., and Ž. Fuchs, 2007: Convectively coupled gravity and moisture modes in a simple atmospheric model. *Tellus*, **59A**, 627–640, <https://doi.org/10.1111/j.1600-0870.2007.00268.x>.
- , and —, 2009: Moisture modes and the Madden–Julian oscillation. *J. Climate*, **22**, 3031–3046, <https://doi.org/10.1175/2008JCLI2739.1>.
- , and —, 2018: The Madden–Julian oscillation and the Indo-Pacific warm pool. *J. Adv. Model. Earth Syst.*, **10**, 951–960, <https://doi.org/10.1002/2017MS001258>.
- , G. B. Raga, C. S. Bretherton, J. Molinari, C. López-Carrillo, and Ž. Fuchs, 2003: Convective forcing in the intertropical convergence zone of the eastern Pacific. *J. Atmos. Sci.*, **60**, 2064–2082, [https://doi.org/10.1175/1520-0469\(2003\)060<2064:CFITIC>2.0.CO;2](https://doi.org/10.1175/1520-0469(2003)060<2064:CFITIC>2.0.CO;2).
- , S. L. Sessions, A. H. Sobel, and Ž. Fuchs, 2009: The mechanics of gross moist stability. *J. Adv. Model. Earth Syst.*, **1**, 9, <https://doi.org/10.3894/JAMES.2009.1.9>.
- Roundy, P. E., and W. M. Frank, 2004: A climatology of waves in the equatorial region. *J. Atmos. Sci.*, **61**, 2105–2132, [https://doi.org/10.1175/1520-0469\(2004\)061<2105:ACOWIT>2.0.CO;2](https://doi.org/10.1175/1520-0469(2004)061<2105:ACOWIT>2.0.CO;2).
- Schiro, K. A., F. Ahmed, S. E. Giangrande, and J. D. Neelin, 2018: GoAmazon2014/5 campaign points to deep-inflow approach to deep convection across scales. *Proc. Natl. Acad. Sci. USA*, **115**, 4577–4582, <https://doi.org/10.1073/pnas.1719842115>.
- Sobel, A. H., 2002: Water vapor as an active scalar in tropical atmospheric dynamics. *Chaos*, **12**, 451–459, <https://doi.org/10.1063/1.1480795>.
- , and C. S. Bretherton, 2003: Large-scale waves interacting with deep convection in idealized mesoscale model simulations. *Tellus*, **55A**, 45–60, <https://doi.org/10.3402/tellusa.v55i1.12084>.
- , and E. Maloney, 2012: An idealized semi-empirical framework for modeling the Madden–Julian oscillation. *J. Atmos. Sci.*, **69**, 1691–1705, <https://doi.org/10.1175/JAS-D-11-0118.1>.
- , and —, 2013: Moisture modes and the eastward propagation of the MJO. *J. Atmos. Sci.*, **70**, 187–192, <https://doi.org/10.1175/JAS-D-12-0189.1>.
- , J. Nilsson, and L. M. Polvani, 2001: The weak temperature gradient approximation and balanced tropical moisture waves. *J. Atmos. Sci.*, **58**, 3650–3665, [https://doi.org/10.1175/1520-0469\(2001\)058<3650:TWTGAA>2.0.CO;2](https://doi.org/10.1175/1520-0469(2001)058<3650:TWTGAA>2.0.CO;2).
- , S. Wang, and D. Kim, 2014: Moist static energy budget of the MJO during DYNAMO. *J. Atmos. Sci.*, **71**, 4276–4291, <https://doi.org/10.1175/JAS-D-14-0052.1>.
- Stechmann, S. N., and S. Hottovy, 2017: Unified spectrum of tropical rainfall and waves in a simple stochastic model. *Geophys. Res. Lett.*, **44**, 10 713–10 724, <https://doi.org/10.1002/2017GL075754>.
- Su, H., and J. D. Neelin, 2002: Teleconnection mechanisms for tropical Pacific descent anomalies during El Niño. *J. Atmos. Sci.*, **59**, 2694–2712, [https://doi.org/10.1175/1520-0469\(2002\)059<2694:TMFTPD>2.0.CO;2](https://doi.org/10.1175/1520-0469(2002)059<2694:TMFTPD>2.0.CO;2).
- Sugiyama, M., 2009: The moisture mode in the quasi-equilibrium tropical circulation model. Part I: Analysis based on the weak temperature gradient approximation. *J. Atmos. Sci.*, **66**, 1507–1523, <https://doi.org/10.1175/2008JAS2690.1>.
- Sukhatme, J., 2014: Low-frequency modes in an equatorial shallow-water model with moisture gradients. *Quart. J. Roy. Meteor. Soc.*, **140**, 1838–1846, <https://doi.org/10.1002/qj.2264>.
- Tian, B., and V. Ramanathan, 2003: A simple moist tropical atmosphere model: The role of cloud radiative forcing. *J. Climate*, **16**, 2086–2092, [https://doi.org/10.1175/1520-0442\(2003\)016<2086:ASMTAM>2.0.CO;2](https://doi.org/10.1175/1520-0442(2003)016<2086:ASMTAM>2.0.CO;2).
- Wang, B., 2012: Theory. *Intraseasonal Variability in the Atmosphere–Ocean Climate System*, 2nd ed., W. K. M. Lau and D. E. Waliser, Eds., Springer, 307–360.
- , F. Liu, and G. Chen, 2016: A trio-interaction theory for Madden–Julian oscillation. *Geosci. Lett.*, **3**, 34, <https://doi.org/10.1186/s40562-016-0066-z>.
- Wheeler, M., and G. N. Kiladis, 1999: Convectively coupled equatorial waves: Analysis of clouds and temperature in the wavenumber–frequency domain. *J. Atmos. Sci.*, **56**, 374–399, [https://doi.org/10.1175/1520-0469\(1999\)056<0374:CCEWAO>2.0.CO;2](https://doi.org/10.1175/1520-0469(1999)056<0374:CCEWAO>2.0.CO;2).
- Wing, A. A., and K. A. Emanuel, 2014: Physical mechanisms controlling self-aggregation of convection in idealized numerical modeling simulations. *J. Adv. Model. Earth Syst.*, **6**, 59–74, <https://doi.org/10.1002/2013MS000269>.
- , —, C. E. Holloway, and C. Muller, 2018: Convective self-aggregation in numerical simulations: A review. *Shallow Clouds, Water Vapor, Circulation, and Climate Sensitivity*, R. Pincus et al., Eds., Springer, 1–25, https://doi.org/10.1007/978-3-319-77273-8_1.
- Wolding, B. O., E. D. Maloney, and M. Branson, 2016: Vertically resolved weak temperature gradient analysis of the Madden–Julian oscillation in SP-CESM. *J. Adv. Model. Earth Syst.*, **8**, 1586–1619, <https://doi.org/10.1002/2016MS000724>.
- Yano, J.-I., and K. Emanuel, 1991: An improved model of the equatorial troposphere and its coupling with the stratosphere. *J. Atmos. Sci.*, **48**, 377–389, [https://doi.org/10.1175/1520-0469\(1991\)048<0377:AIMOTE>2.0.CO;2](https://doi.org/10.1175/1520-0469(1991)048<0377:AIMOTE>2.0.CO;2).
- , and R. Plant, 2012: Convective quasi-equilibrium. *Rev. Geophys.*, **50**, RG4004, <https://doi.org/10.1029/2011RG000378>.
- Yasunaga, K., and B. Mapes, 2012: Differences between more divergent and more rotational types of convectively coupled equatorial waves. Part I: Space–time spectral analyses. *J. Atmos. Sci.*, **69**, 3–16, <https://doi.org/10.1175/JAS-D-11-033.1>.
- , S. Yokoi, K. Inoue, and B. E. Mapes, 2019: Space–time spectral analysis of the moist static energy budget equation. *J. Climate*, **32**, 501–529, <https://doi.org/10.1175/JCLI-D-18-0334.1>.
- Yu, J.-Y., and J. D. Neelin, 1994: Modes of tropical variability under convective adjustment and the Madden–Julian oscillation. Part II: Numerical results. *J. Atmos. Sci.*, **51**, 1895–1914, [https://doi.org/10.1175/1520-0469\(1994\)051<1895:MOTVUC>2.0.CO;2](https://doi.org/10.1175/1520-0469(1994)051<1895:MOTVUC>2.0.CO;2).
- , C. Chou, and J. D. Neelin, 1998: Estimating the gross moist stability of the tropical atmosphere. *J. Atmos. Sci.*, **55**, 1354–1372, [https://doi.org/10.1175/1520-0469\(1998\)055<1354:ETGMSO>2.0.CO;2](https://doi.org/10.1175/1520-0469(1998)055<1354:ETGMSO>2.0.CO;2).
- Zeng, N., J. D. Neelin, and C. Chou, 2000: A quasi-equilibrium tropical circulation model—Implementation and simulation. *J. Atmos. Sci.*, **57**, 1767–1796, [https://doi.org/10.1175/1520-0469\(2000\)057<1767:AQETCM>2.0.CO;2](https://doi.org/10.1175/1520-0469(2000)057<1767:AQETCM>2.0.CO;2).
- Zhang, C., 2005: Madden–Julian oscillation. *Rev. Geophys.*, **43**, RG2003, <https://doi.org/10.1029/2004RG000158>.